MAX-PLANCK-INSTITUT FÜR PHYSIK UND ASTROPHYSIK
WERNER-HEISENBERG-INSTITUT FÜR PHYSIK

MPI-PAE/Exp. El. 143
November 1984

FORWARD PARTICLE PRODUCTION IN π^-p and K^-p COLLISIONS AT 58 GeV/c AND COMPARISON WITH QUARK MODELS

The ACCMOR Collaboration

F. Pauß[4X], A. Gonzalez-Arroyo[2+], W. Ochs[4], B. Alper[6↔], G. Blanar[4@], M. Cerrada[4§], V. Chabaud[2], C. Damerell[6], C. Daum[1], H. Dietl[4], A. Gillman[6], C. Hardwick[6°], W. Hoogland[1], R. Klanner[4†], J. Loken[5], E. Lorenz[4], G. Lütjens[4], G. Lutz[4], W. Männer[4], G. Polok[3], M. Rozanska[3], W. Spalding[5□], U. Stierlin[4], G. Thompson[5‡], H. Tiecke[2*], J. Turnau[3], P. Weilhammer[2] and F. Wickens[6]

Abstract

We present single inclusive $\pi^{\pm}$, π^{o} and $K^{\pm}$ spectra in the forward fragmentation region ($x > 0.2$, $p_T < 1.5$ GeV/c) as well as correlations between two charged particles. The data were recorded in an unseparated negative hadron beam at the CERN SPS using a large acceptance forward spectrometer. Our measurements are compared in detail with several models which emphasise the role of the beam valence quarks in this production process. The connection to measurements at large p_T is also investigated.

Submitted to Zeitschrift für Physik C

---

1 NIKHEF-H, Amsterdam, The Netherlands.
2 CERN, Geneva, Switzerland.
3 Institute of Nuclear Physics, Cracow, Poland.
4 Max Planck Institut für Physik, Munich, Fed. Rep. Germany.
5 University of Oxford, Oxford, UK.
6 Rutherford Laboratory, Chilton, Didcot, UK.
x Now at CERN, Geneva, Switzerland.
+ Now at the Univ. Autonoma de Madrid, Madrid, Spain
↔ Now at ETSU, Harwell, England.
@ Now at LeCroy Research Systems, Geneva, Switzerland.
§ Now at the Junta de Energia Nuclear, Madrid, Spain.
° Now at Culham Laboratory, Abingdon, UK.
† Now at DESY, Hamburg, Fed. Rep. Germany.
□ Now at FNAL, Batavia, USA.
‡ Now at Queen Mary College, University of London, England.
* Now at NIKHEF-H, Amsterdam, The Netherlands.

8000 MÜNCHEN 40 - FÖHRINGER RING 6

FORWARD PARTICLE PRODUCTION IN π^-p and K^-p COLLISIONS AT 58 GeV/c AND COMPARISON WITH QUARK MODELS

The ACCMOR Collaboration

F. Pauß[4X], A. Gonzalez-Arroyo[2+], W. Ochs[4], B. Alper[6↔],
G. Blanar[4@], M. Cerrada[4§], V. Chabaud[2], C. Damerell[6],
C. Daum[1], H. Dietl[4], A. Gillman[6], C. Hardwick[6°]
W. Hoogland[1], R. Klanner[4†], J. Loken[5], E. Lorenz[4],
G. Lütjens[4], G. Lutz[4], W. Männer[4], G. Polok[3],
M. Rozanska[3], W. Spalding[5□], U. Stierlin[4], G. Thompson[5‡]
H. Tiecke[2*], J. Turnau[3], P. Weilhammer[2] and F. Wickens[6]

Abstract

We present single inclusive $\pi^{\pm}$, π^{o} and $K^{\pm}$ spectra in the forward fragmentation region ($x > 0.2$, $p_T < 1.5$ GeV/c) as well as correlations between two charged particles. The data were recorded in an unseparated negative hadron beam at the CERN SPS using a large acceptance forward spectrometer. Our measurements are compared in detail with several models which emphasise the role of the beam valence quarks in this production process. The connection to measurements at large p_T is also investigated.

Submitted to Zeitschrift für Physik C

---

1 NIKHEF-H, Amsterdam, The Netherlands.
2 CERN, Geneva, Switzerland.
3 Institute of Nuclear Physics, Cracow, Poland.
4 Max Planck Institut für Physik, Munich, Fed. Rep. Germany.
5 University of Oxford, Oxford, UK.
6 Rutherford Laboratory, Chilton, Didcot, UK.
× Now at CERN, Geneva, Switzerland.
+ Now at the Univ. Autonoma de Madrid, Madrid, Spain
↔ Now at ETSU, Harwell, England.
@ Now at LeCroy Research Systems, Geneva, Switzerland.
§ Now at the Junta de Energia Nuclear, Madrid, Spain.
° Now at Culham Laboratory, Abingdon, UK.
† Now at DESY, Hamburg, Fed. Rep. Germany.
□ Now at FNAL, Batavia, USA.
‡ Now at Queen Mary College, University of London, England.
* Now at NIKHEF-H, Amsterdam, The Netherlands.

1. INTRODUCTION

A large effort has been devoted in recent years to the detailed experimental study of hadron production in hard processes, such as e^+e^- annihilation, deep inelastic lepton scattering and large p_T hadron hadron collisions. The basis for the theoretical understanding has been provided by the quark parton model and a more refined analysis has been carried out by applying Quantum-chromodynamics (QCD) in some approximate way.

Much less became known about the details of particle production in soft hadron hadron collisions which build up the large total hadronic cross-section, and the theoretical understanding based on the parton model or even QCD is still in its infancy, if compared to the hard processes. This may be due to the fact that in soft collisions a large momentum transfer scale Q^2, which one usually refers to in applying the parton model, is not easily identified.

A successful phenomenological approach has been provided by the Triple Regge model. Here the quarks do not appear as elementary objects in phase space, rather the Regge trajectory, a certain sequence of hadronic states, appears as the basic entity. Though this model has been very successful in the description of selected inclusive spectra in a restricted region of phase space (when a single Regge trajectory can be exchanged), a more complete view of multiparticle phenomena at small p_T is still lacking and the relation to a fundamental theory has not yet been elaborated.

In another class of models quarks are considered as real objects in phase space which interact with one another to yield the final hadronic states. An early model of this kind predicted the ratio of total cross-sections $\sigma_{\pi p}/\sigma_{pp} = 2/3$ from the number of constituent valence quarks [1]. A discussion of the more recently developed quark models for soft multiparticle production is given in the review articles by Collins and Martin [2], Fialkowski and Kittel [3] and at a 1981 Erice Conference [4].

In this experiment we studied forward particle production in π^-p and K^-p collisions at 58 GeV/c. We present results on x and p_T spectra of charged pions and kaons and neutral pions as well as charged particle correlations.

We will compare our data to the following models (applying the classification of ref. [3]), where we restrict ourselves to a discussion of the simplest original ideas:

(1) Quark combinatorics and additive quark model [5,6],

(2a) Fragmentation model [7],

(2b) Dual parton model [8,9],

(3) Recombination model [10-13] and

(4) Quark counting rules [14,15].

Our data will be relevant in particular for the fragmentation models (2a), (2b) which relate the soft forward production to the quark fragmentation observed in hard processes.

Two other experiments have presented data on single inclusive spectra of identified particles. Charged particles have been measured using a single arm spectrometer [16] for a set of fixed x, p_T values but covering a smaller solid angle than our experiment. A CALTECH-LBL group [17] has measured π^o's with higher statistics and extending to larger p_T values than our experiment, but without presenting inclusive x spectra. The advantage of our experiment is the simultaneous measurement of charged and neutral particle spectra in the same spectrometer at the same beam energy and also the ability to measure multiparticle correlations, which allows more stringent tests of the models considered.

In Section 2 we describe our apparatus and experimental procedures. Section 3 is devoted to the discussion of x spectra and comparison to the various quark models. In Section 4 we give an account of our p_T spectra together with some phenomenological remarks. In Section 5 we attempt to distinguish further between fragmentation and recombination models using correlation data, and we draw some conclusions in Section 6.

2. APPARATUS AND DATA ANALYSIS

2.1 The Spectrometer

The ACCMOR spectrometer was located in the H1b beam of the CERN SPS (experiment WA3). A schematic view of the spectrometer in the configuration used for this experiment is shown in Fig. 1. It consists of the following basic elements:

(a) Beam spectrometer. Incident beam particles were identified by two differential CEDAR Cerenkov counters and one threshold Cerenkov counter (BC); their direction has been measured by two sets of multiwire proportional chambers (Arm IV a,b). A set of scintillation counters defined the useful beam (UB).

(b) A 50 cm liquid hydrogen target (T).

(c) A forward magnetic spectrometer for the determination of particle momenta, consisting of two wide gap magnets and several sets of wire spark chambers with magnetostrictive readout (Arm Ia,b,II,IIIa,b,c). The purpose of the first magnet M1 (bending power 0.85 Tm and $2 \times 0.4\ m^2$ window) was to measure particles between 0.5 and about 5 GeV/c with sufficient precision, while the very fast forward going secondary particles were measured with the magnet M2 (2.0 Tm and $1.5 \times 0.5\ m^2$ window).

(d) Two threshold Cerenkov counters (C1, C2), matching the exit window of the second magnet for particle identification. The counters were subdivided into 14 and 16 cells respectively and operated at atmospheric pressure.

(e) A fine grain γ-calorimeter for π^0 detection at the end of the detector, about 25 m behind the target. The calorimeter consisted of two identical blocks with alternating layers of lead and scintillator; each block segmented horizontally and vertically into 70 strips. The calorimeter covered a total area of $3 \times 1.5\ m^2$ transverse to the beam. The energy of a single electromagnetic shower was obtained independently from both projections. More details on construction and operation of this calorimeter are given elsewhere [18].

(f) A small scintillation counter D ($4 \times 6\ cm^2$) located on the beam trajectory 8.5 m downstream of the target centre sensed the non-interacting beam, and was used in the interaction trigger.

(g) Associated fast electronics for the trigger selection and online computer.

Further details of the detector can be found in ref. [19].

2.2 Data Taking, Reconstruction and Selection of Events

In order to measure fully inclusive particle spectra we had to record all interactions in the target. This was achieved by an interaction trigger which required a beam particle in the beam telescope UB together with an anticoincidence signal from the D counter to suppress events with non-interacting beam. In addition a signal from the beam Cerenkov counters was required either in one of the CEDAR counters for incident kaons or in the threshold Cerenkov counter for incident pions. To enrich the kaon sample a gate for the pion trigger was only opened for 5% of the time at the end of the beam spill.

In 3½ days a total of 369 k pion-induced and 271 k kaon-induced interactions were recorded. The identification of secondary particles by Cerenkov counters was only possible for part of the data corresponding to 152 k pion beam and 104 k kaon beam triggers. The data analysis proceeded in general along the lines already described previously in the study of diffractive three particle production [19]. To derive inclusive spectra a wider range of event topologies had to be treated and in the remaining part of this section we discuss some essential parts of our analysis which had to be developed or altered for this purpose.

The events were processed with the reconstruction program TENPRO [19] which allows up to 10 reconstructed tracks in the forward direction. Losses for higher multiplicities were found to be less than 1%. The program constructed a primary vertex connecting the beam track with those secondary tracks which came sufficiently close according to a χ^2 criteria. The loss of tracks by the fitting procedure was estimated to be less than 2%. Events without a primary vertex fit were contained in the sample as candidates for multineutral production.

An event was rejected, if

(a) the primary vertex was found outside the hydrogen target (~ 30%). Multineutral events without a primary vertex fit were rejected if there was a beam-like track in arm I (angle $\Theta < 0.7$ mrad to the beam track in arm IV) to minimize the number of interactions outside the target;

(b) an additional beam track passed the target within the memory time of the spark chambers (~ 10%);

(c) the beam track could not be reconstructed (2%).

Finally a total of 206 k pion-induced and 145 k kaon-induced events remained, out of which 76 k pion beam and 60 k kaon beam events had Cerenkov identification of secondary particles. For 85% of these events a primary vertex was reconstructed. In calculating the absolute normalisation corrections were applied to compensate for the various cuts; the total calibration uncertainty was estimated to be 8%.

2.3 Geometrical Acceptance

As our detector did not have a full coverage of the solid angle, the observed data had to be corrected for losses in geometrical acceptance. Our particle spectra are described in terms of the two variables $x = p_{||}/p_{lab}$, the longitudinal momentum fraction and p_T, the transverse momentum. The acceptance $A(x,p_T)$ was calculated in a fine grid of x and p_T values by generating the beam according to the measured profiles, the appropriate vertex positions inside the target and the secondary particle with random rotation around the beam axis. The acceptance for a pair of x, p_T values was determined as the fraction of tracks which would pass the various windows as defined by the size of the detector elements.

In this paper we present results on identified charged particles and also on unidentified charged particles. In order to identify the particles by Cerenkov counters we require the tracks to be reconstructed within the smaller aperture of the detector defined by both magnets and all spark chambers. If we are not interested in particle identification, we can include all particles which leave the target into the larger aperture defined by the first magnet and the arm I and arm II chambers alone. In Fig. 2 we show as a result of our acceptance calculations the limits A = 100% (full acceptance) at small angles and A = 0% (no acceptance) at large angles for both cases. Between these limits the acceptance varies almost linearly. The D counter causes the acceptance hole around $x = 1$, $p_T = 0$ for negative (beam-like) particles, whereas for positive particles this counter decreases the acceptance by about 10% in a wider band of x and p_T (not shown in Fig. 2).

As a check of our acceptance calculation we determined inclusive spectra from tracks accepted by both the smaller and the larger aperture configurations, using the respective correction tables and we found good agreement.

In the case of our charged particle correlation measurements, it turned out that the total acceptance could be calculated as the product of the respective single particle acceptances.

2.4 Particle Identification by Cerenkov Counters

The secondary charged particles were identified using the light signals they produced in the cells of the counters. Corrections have to be applied (a) for ambiguities when several particles are associated with the same cell and (b) for inefficiencies of the counters.

An additional track in the same cell may come from another particle produced at the primary vertex inside the target or also by secondary interactions in the detector material; in the second case the momentum of the track is not always known. For each track the information from the two Cerenkov counters i = 1,2 can be summarised by a pair of numbers (n_1, n_2), where $n_i = 0,1,A$ refers to a track which gives no light, gives light or is ambiguous in the respective cell. For each x and p_T bin we can then determine the corresponding observed numbers of tracks $N^{ob}_{n_1 n_2}$, the total sum being denoted by N. Then we define the probability p^1_A for a track to be ambigous in C1 but unique in C2, similarly p^2_A, and finally p^{12}_A to be ambiguous in both counters by

$$p^1_A = (N^{ob}_{A0} + N^{ob}_{A1})/N;$$

$$p^2_A = (N^{ob}_{0A} + N^{ob}_{1A})/N; \qquad (2.1)$$

$$p^{12}_A = N^{ob}_{AA}/N$$

All probabilities were found to decrease with increasing x; at x = 0.2 (after summing over p_T) we found $p^1_A = 0.16$, $p^{12}_A = 0.03$ and $p^2_A = 0.005$, at x = 0.6 $p^1_A = 0.07$ and p^2_A, $p^{12}_A \leq 0.003$ whereas at $x \geq 0.8$ all probabilities $p_A < 0.001$. Under the assumption that these ambiguity classes are approximately independent we can write

$$N^{ob}_{ik} = (1-p^1_A)(1-p^2_A)(1-p^{12}_A)\, N_{ik} \qquad (2.2)$$

$$\approx (1-p^1_A-p^2_A-p^{12}_A)\, N_{ik}$$

where i,k = 0,1 for no light, light in C1,C2.

Then we can determine the "true" number of tracks N_{ik} from the observed ones by an appropriate scale factor. The p_T dependence of this scale factor as well as its dependence on the type of beam or secondary particle was found to be less than 25% around the mean value at a given x.

There were a small fraction of particles which -- though fully momentum analysed -- did not yield a sufficiently well reconstructed track in arm IIIc at the end of the detector along the expected trajectory. These tracks have been classified as ambiguous too. They represent typically a fraction of 7% of the total number of tracks, but this fraction could increase up to ~ 20% at small $p_T < 0.2$ GeV/c which is due to an inefficiency of the chambers near the position of the non-interacting beam.

The uncertainty of the correction for the ambiguous tracks has been taken into account in the error determination. We added 25% of the full correction in quadrature to the statistical error.

From the numbers N_{ik} one can derive the numbers N_h of hadrons of type h in each x, p_T bin, taking into account the efficiencies e_i^h of the Cerenkov counter i. The threshold momenta p_{th}^h are given in Table 1 and we can neglect e_1^p, e_2^p and e_2^K. (The small probability for a particle to give light below or near threshold will be left out here for simplicity, though it has been taken into account in the analysis if necessary.) Then we obtain

$$\text{(a)} \quad N_{00} = (1-e_1^\pi)(1-e_2^\pi)N_\pi + (1-e_1^K)N_K + N_p$$

$$\text{(b)} \quad N_{11} = e_1^\pi e_2^\pi N_\pi \qquad (2.3)$$

$$\text{(c)} \quad N_{10} = e_1^\pi(1-e_2^\pi)N_\pi + e_1^K N_K$$

$$\text{(d)} \quad N_{01} = (1-e_1^\pi)e_2^\pi N_\pi$$

First we can determine e_1^π from (2.3 b,d) for $p > p_{th}^\pi$ (C2) and e_2^π from (2.3 b,c) for p_{th}^π (C2) $< p <$ p_{th}^K (C1). The results are shown in Fig. 3 as triangles together with another determination in the same experiment based on a large sample of identified pion pairs [19]. Good agreement is found. The data fitted to the formula $e_i(p) = 1-\exp[-\bar{n}_i(1-(p_{th}/p)^2)]$ as expected with $\bar{n}_1 = 5.2$ and $\bar{n}_2 = 5.8$ photoelectrons produced for $p \to \infty$ respectively.

The number of pions has then been determined for $11.6 < p < 25$ GeV/c ($e_1^K \approx 0$) from $N_{11} + N_{10} = e_1^\pi N_\pi$ and for $p > 25$ GeV from eq. 2.3b, whereas the number of kaons for $p > 29$ GeV/c ($x > 0.5$) could then be found from 2.3c. Because of the small efficiency e_1^K near threshold we required usually $x > 0.6$, except for the large rates of $K^- \to K^-$. The number of protons could be determined from 2.3a; we found $N_p \leqq N_K$ but because of large errors we did not pursue this analysis.

Finally the data have been corrected for the loss of tracks from secondary interactions (9%) and in case of secondary kaons for decay. An important background for the reaction $K^- p \to \pi^-$, in particular for large x was due to decays of the beam kaon $K^- \to \mu^- \nu$, $\pi^- \pi^0$. These decays could be seen as clear peaks in the missing mass spectra and therefore be removed from the inclusive distributions.

2.5 π^0 Detection

The neutral pions have been reconstructed from the photon calorimeter data in 4 steps.

(1) Shower recognition. A shower was defined as a peak in the energy deposition in either horizontal or vertical detector elements. Three adjacent elements were used to determine the total shower energy. These elements are known to contain 95% of this energy. As we are primarily interested in fast π^0's, we removed a large part of the background from various sources by an initial cut of 3 GeV on the shower energy.

(2) Removal of hadron showers. One third of the hadrons entering the calorimeter produced a shower of at least 3 GeV. These hadron showers can be identified, since their location can be extrapolated from the measured trajectories of charged hadrons. However, part of the time, a photon shower overlapped with a hadron shower in one projection. To avoid losing photons with energy greater than 8 GeV, we did not remove those hadron showers for which the horizontal and vertical energy determinations differed by more than 7 GeV.

(3) Reconstruction of photons. A pair of showers in horizontal and vertical projections with respective energies E_H and E_V has been associated to a photon if their energies were sufficiently close. We required

$$K^2 = \left(\frac{E_H - E_V}{E_H + E_V} \right)^2 < 0.04$$

From a sample of unambiguously identified π^0's we estimated the loss of good photons due to this cut to be < 1%. Less frequently there was the case of photon overlapping, where two photons yield two showers with energies E_1, E_2 in one projection but only one shower of energy E_{ov} in the other projection. Then we required

$$\tilde{K}^2 = \left(\frac{E_{ov} - E_1 - E_2}{E_{ov} + E_1 + E_2} \right)^2 < 0.08$$

corresponding to a loss of good events of $< 4\%$. In order to find the photons in one event which fitted the observed pattern of showers in both projections we proceeded as follows: (a) we tried all possible combinations from both projections and applied the above criteria to find photon candidates. In about 60% of events a unique solution was found where all showers have been related to photons. (b) For the remaining events it was checked whether some unpaired showers could be explained by other reasons (loss of one projection due to edge or threshold effects, secondary hadron showers and others). Then we have chosen the combination with the smallest number of unexplained peaks. (c) In the remaining 20% of events there were more than one (mostly two) competitive solutions. This includes events with two photons of comparable energies where however both possible combinations would yield the same π^0 momentum vector. For this category of events we have chosen one possibility at random.

We found that the ambiguities in (b) and (c) came primarily from photons of low energy. We therefore included in our final sample only those photons with energies exceeding 8 GeV. With this restriction the loss of good photons from our procedure was negligible.

(4) Determination of inclusive π^0 spectra. The invariant mass spectrum of all two photon combinations is shown in Fig. 4a and a clear π^0 signal is seen. The π^0 mass resolution is found to be $\sigma \sim 8$ MeV. To obtain the final inclusive spectra the background under the peak was subtracted for each bin in x and p_T; furthermore, corrections have been applied for geometrical acceptance which limits the p_T spectra to $p_T < 0.8$ GeV/c, for the energy cutoff of 8 GeV of the photons, and for the loss of photons (17%) by conversion into e^+e^- pairs in the material between the target and the second bending magnet. The decays $K^- \to \pi^-\pi^0$ could be again removed by inspection of the $\pi^-\pi^0$ invariant mass distribution. We expect 12% of the multineutral events without primary vertex fit to come from interactions outside the target (but not behind arm Ia according to our event selection); the fraction of such events increases with x and we obtain a correction of 1% for $x = 0.45$ and of 7% for $x = 0.95$.

Finally we emphasize two consistency checks of our reconstruction procedure: (a) we looked at the energy distribution of γ's which came from the decay of a π^o with energy E_{π^o}. As expected this distribution is flat between 8 GeV $< E_\gamma < E_{\pi^o}/2$, see Fig. 4b-d for 3 intervals of E_{π^o} (the drop below the dashed line is due to the finite interval of E_{π^o}) and there is no indication of an energy dependent loss of photons; (b) we varied the lower cutoff in the photon energy from 8 GeV to 7 GeV and to 6 GeV respectively. We found that the appropriately corrected final x distributions agreed with each other both in shape and normalisation. This shows that our reconstruction program works well even for a smaller energy cutoff.

3. INCLUSIVE x-DISTRIBUTIONS

3.1 The Data

Our basic results on the p_T integrated invariant cross-sections

$$\sigma_{in}\, \rho(x) = \int E \frac{d\sigma}{d^3p}\, dp_T^2 \approx \frac{x}{\pi} \frac{d\sigma}{dx} \tag{3.1}$$

are presented in Fig. 5 and Table 2 as a function of scaled longitudinal momentum

$$x = p_{||}/p_{lab} \tag{3.2}$$

evaluated in the lab frame. If we had chosen the CM frame instead, the data points would decrease at most at $x = 0.2$ by 2%. For the convenience of the reader we show in Fig. 6 how the kinematical quantities in both frames are related. In (3.1) we define to the spectra $\sigma_{in}\, \rho(x)$ normalised to the total inelastic cross-sections. We refer later to the $\rho(x)$ using $\sigma_{in}^{\pi^- p} = 20.8$ mb and $\sigma_{in}^{K^- p} = 17.8$ mb. For charged particles the integral in (3.1) is performed by collecting all tracks with a weight correcting for geometrical acceptance and other losses: The acceptance hole of negative particles with $0.7 < x < 0.9$ (for leading particles $x < 0.95$) and $p_T < 0.2$ GeV/c due to the D-counter is corrected for by extrapolating our fits to the observed p_T spectra as explained in Section 4 below (correction smaller than 15%), whereas the data with $x > 0.9$ (0.95 resp.) are dropped. The π^o spectra could only be measured up to $p_T = 0.8$ GeV/c due to the limited acceptance of our calorimeter. Again we used our fits (Section 4) to correct for pions with $p_T > 0.8$ GeV/c, which yields a maximal correction of 25% at $x = 0.4$. Kaons are only included for $x > 0.6$ where a complete separation from pions and protons were possible with good efficiency; in the case of reaction $K^- \to K^-$ with its high rate the limit could be lowered to $x = 0.5$.

Finally we want to compare our results with those obtained by other groups. Single inclusive spectra of charged particles for various incident beam particles have been determined for several settings of a single arm spectrometer [16] which yields cross-sections for a grid of x-p_T values. By fitting the p_T spectra to a parametric form inclusive x-spectra have also been derived. In general our results from the interaction trigger experiment agree reasonably well in the overlapping regions, except that our pion spectra increase a bit faster towards small x for $x < 0.6$ with a discrepancy of 20% in normalisation at $x = 0.2$ (see Fig. 7). For comparison we also show results from a bubble chamber experiment at 40 GeV/c [20] where particle identification is only possible for slow particles and the pion spectra could have a proton contamination of 15%. These measurements as well as similar results from Whitmore et al. at 100 GeV/c [21] (not shown) are in good agreement with ours.

3.2 Comparison with Quark Models

In this section we will compare our results on inclusive x distributions with the predictions from four types of models which emphasize the role of valence quarks in particle production at low p_T: (1) Quark combinations (2a) Fragmentation model (2b) Dual Parton model (3) Recombination model and (4) counting rules. It should be noted that the nature of the predictions from these models is quite different. They do not usually refer to the same experimental quantities, rather each model refers to particular aspects of the data. Model (1) predicts an overall ordering of the rates of the various spectra and certain particle ratios for large x but not the shape of the distributions. Models (2a,b) predict all x-spectra in terms of quark fragmentation functions which are in principle measurable in hard processes but are actually not all known, so that one takes these functions from parametrizations adjusted to available data. Model (3) relates the x-spectra to the various quark structure functions of the beam particle which in our case of meson beams are only partly known from lepton pair production measurements, so that not many direct predictions apply to our data. The counting rules finally predict the shape of the x distributions for large x without giving the relative rates. In the following four subsections we give in turn a short account of these models and compare their predictions with our data. It turns out that the most detailed predictions for our data come from the fragmentation models (2a),(2b), therefore the major part of our discussion will concentrate on those.

3.2.1 Quark Combinatorics

We consider first the statistical quark model as worked out by Anisovich and Shekhter [6]. In this model one valence quark of the incident meson, which carries in average half of the beam momentum, interacts with one quark of the target and thereby a sea of new quark pairs is produced. The remaining quarks fly through as spectators and recombine with the sea quarks. The yield of fast hadrons then depends on the number of valence quarks they have in common with the beam particle. In our case of meson beam we can define three classes: class VV for particles with two common valence quarks (leading particle transitions $H \to H$), class VS for particles with one valence, one sea quark and class SS for particles with two sea quarks.

The model has two types of predictions. First, one expects the rates for the different classes to be ordered like (VV)>(VS)>(SS). Second, the relative production rates in classes (VV) and (VS) are predicted from statistical considerations. For example, one obtains $(K^- \to \pi^o)/(\pi^- \to \pi^o) = ½$ as only the $\bar{u}$ quark in the K^- but both valence quarks in the π^- can recombine with a sea quark to produce a π^o. The suppression of kaons over pions is related in this model to the small ratio λ of the probability to pick up a strange quark over the probability to pick up a non-strange quark from the sea.

In Fig. 8 we show the normalised spectra $\rho(x)$ for the above three classes. The predicted relative statistical weights by which the spectra in the (VV) and (VS) classes should appear is also given in the figure. At $x \sim 0.5$ which corresponds to the average momentum of the spectator quark the above inequality for the rates in the three classes reads for pions $0.8 > 0.5 > 0.25$ whereas the heavier kaons are further suppressed by up to a factor of 5. Only at $x \sim 0.9$ the three classes become very distinct and are separated by one order of magnitude in rate. An exception is the transition $\pi^- \to \pi^+$ which behaves like class VS for $x < 0.9$. This is presumably a reflection of diffractive A_1 production as discussed in more detail in the next subsection.

Turning now to the relative rates within one class, we see in Fig. 8 that the three appropriately weighted VS pion spectra fall within a band where the maximal deviation of points is by a factor of 2. Also the VV transition $\pi^- \to \pi^-$ falls into this band for $x \leq 0.6$, but for larger x the diffractive contribution takes over. To

reveal more clearly these predictions of the model we compare in Fig. 9 (a) the ratios of the pion (VS) spectra and in (b) some K/π ratios with the predicted values (dashed lines) using the statistical weights as in Fig. 8 and choosing a central value $\lambda = 0.3$. Some systematic deviations are seen to occur. If one applies the model to the "direct" production of pseudoscalar mesons and production of vector mesons with a relative statistical weight 1:3, as proposed already by Anisovich and Shekhter, the predictions become clearly more complicated, but one may argue that the direct production of mesons dominates near $x = 1$ over the indirect production from vector meson decays, and the ratios should approach the predicted values for large x. It can be seen however that the ratio $(K^- \to \pi^o)/(\pi^- \to \pi^o)$ misses the predicted value by $\sim 40\%$. In summary the model accounts for the general characteristics of our spectra but some systematic deviations are also seen to occur.

3.2.2a Quark Fragmentation Model

In the original formulation of this model [7] one valence quark of the meson beam particle interacts with small momentum ($x \approx 0$) whereas the other quark carries the full momentum ($x \approx 1$) and then fragments as in deep inelastic processes ("quark stripping"). The forward hadronic jet can then be looked at as an incoherent superposition of two quark jets initiated by either one of the two valence quarks in the beam. Our inclusive hadron spectra can therefore be related to the respective quark decay functions $D_q^H(x)$ which represent the x-distribution of hadron H from quark q as measured in hard processes according to

$$\pi p^{\pi^- \to H'}(x)/x = \tfrac{1}{2}\,(D_{\bar{u}}^{H'}(x) + D_d^{H'}(x)) \qquad (3.3a)$$

$$\pi p^{K^- \to H'}(x)/x = \alpha\; D_{\bar{u}}^{H'}(x) + \beta\, D_s^{H'}(x) \qquad (3.3b)$$

with $\alpha = 1-\beta = 0.4$. The different weights α,β in the latter case are due to the s quark proton scattering being smaller than the u quark proton scattering so that s quark fragmentation is enhanced. Two difficulties occur, if we want to compare this model to our data.

(a) Diffraction dissociation: The model applies to the non diffractive collisions only and we should subtract the diffractive events. Restricting to single diffraction we get a contribution from the target break-up which yields the forward peak in the VV transitions $H \to H$. Furthermore we have contributions due to the beam break-up which may spread over various channels. If the diffractive mass is large enough, one expects that the decay products are distributed as in the non diffractive events*) but for low masses considerable distortions of the decay spectra may occur. For example the unusually large rate of $\pi^- \to \pi^+$ at large x is due to the chain $\pi^- \to A_1^-$ ($A_1^- \to \rho^0 \pi^+$; $\rho^0 \to \pi^+ \pi^-$) [23]. As we cannot separate diffractive events experimentally because of our limited acceptance, we have chosen not to apply any correction at all and therefore we have to keep in mind the possibility of distortions by diffractive events. In pp collisions [22] this distortion can be estimated to be smaller than 20% (after extrapolation to our beam energy). Removing diffractive events would make the spectra flatter in that case.

(b) Quark decay functions: These distributions can be measured in principle in deep inelastic scattering, but they are not all known, as e.g. s-quark fragmentation. We have therefore used on the r.h.s. of eq. 3.3 the parametrisation of quark jets proposed by Field and Feynman [24] who use of data where available and incorporate various symmetries based on the quark composition of hadrons in a recursive scheme of fragmentation. Furthermore the model exhibits the approximate relations

$$\text{(a) } D_s^{\pi^\pm} \approx D_u^{\pi^-} \qquad \text{(b) } D_s^{K^+} \approx D_u^{K^-} \tag{3.4}$$

For our comparison we take their Monte Carlo generated spectra which in the region of low statistics may have an uncertainty of up to 50%.

The π^0 spectra we calculate from

$$D_q^{\pi^0} = \tfrac{1}{2} (D_q^{\pi^+} + D_q^{\pi^-}) \tag{3.5}$$

For later use we also define

$$R_u = D_u^{\pi^-} / D_u^{\pi^+} \tag{3.6}$$

where $R_u \to 0$ for $x \to 1$.

---

*) It has been observed at the ISR that particle production in one hemisphere is largely uncorrelated with the proton momentum in the other hemisphere [22].

Two further comments on the Field Feynman model are in order. First, the model contains the s-quark suppression factor λ as a free parameter. In the original calculations the value $\lambda = 0.5$ has been chosen based on an analysis of the K^+/π^+ ratio at large p_T in pp collisions within a quark quark scattering model. Other model dependent determinations have yielded the smaller value $\lambda \approx 1/3$ [25] but in a recent determination directly from the quark fragmentation in νp scattering the value $\lambda \approx 0.2$ is obtained [26]*). Therefore the Field Feynman model with $\lambda \approx 0.5$ presumably overestimates the kaon yield by roughly a factor of 2. Secondly, as the fragmentation functions depend in general on some scale Q^2 one should compare different reactions at similar scales. This appears to be reasonably satisfied as the data which enter the Field Feyman fits and our data are in the range of total energy $3 < \sqrt{s} < 10$ GeV.

We now turn to the comparison of our data with the appropriate combination of decay functions as in eqs. 3.3 in Fig. 10. Disregarding the forward diffractive peaks for $x > 0.6$ the overall agreement based on this simple ansatz is quite remarkable. An exception is the shoulder seen in $\pi^- \to \pi^+$ in the range $0.6 < x < 0.95$ which may be explained by diffraction dissociation. Otherwise the predictions for pions work quite well (within 30%); for kaons the shape is predicted correctly though the normalisation is too high by about a factor 2. We anticipate that the smaller value $\lambda \approx 0.2$ suggested by νp data as emphasised above would improve the agreement also for the normalisation of the kaon spectra.

It is again instructive to study particle ratios. Here a normalization uncertainty from diffractive events and also some possible scale breaking effects may largely cancel. In Fig. 11 we show ratios for particles with the same mass. They all approach 1 for $x \to 0$ in the model and the uncertainty in λ drops for $x \to 1$.

The VS/VS ratios in Fig. 11a approach a constant value for $x \to 1$ as in the above statistical model (1) and we can see how its simple predictions are modified. We find with eqs. (3.3-3.6)**) in the limit $x \to 1$

$$\frac{K^- \to \pi^0}{K^- \to \pi^-} = \frac{\alpha/2 + (1-\alpha/2)\, R_u}{\alpha + (1-\alpha)\, R_u} \to \frac{1}{2} \qquad (3.7)$$

as before, whereas the ratio

$$\frac{K^- \to \pi^0}{\pi^- \to \pi^0} = \alpha + 2(1-\alpha)/(1+R_u^{-1}) \to \alpha = 0.4 \qquad (3.8)$$

---

*) The large value for the K/π ratio in pp collisions can possibly be related to the observed increase of the K/π ratio with p_T within a quark jet [26].

**) The ratios which follow refer to the ratios of normalised distributions $\rho(x)$ in (3.1).

reflects the different weight of s and u fragmentation in the K^- at large x where all the data fall below the statistical prediction of 1/2. It is not possible to improve the agreement with data by choosing a smaller value $\alpha = 0.3$ as one would run into conflict with data on the ratio

$$\frac{K^- \to \pi^+}{K^- \to \pi^-} = \frac{R_u}{\alpha+\beta R_u} \to \frac{1}{\alpha} R_u \qquad (3.9)$$

(see Fig. 11b): here the model curve would increase, away from the data. Indeed, in the limit $\alpha = 0$ (only s-quark fragmentation) the isospin symmetry would require this ratio to be 1 throughout. A considerable $\bar{u}$ quark fragmentation is therefore required and the model with $\alpha = 0.4$ comes rather close to the data though some discrepancy remains.

A similar x dependence is found in the other ratio displayed in Fig. 11b

$$\frac{\pi^- \to K^+}{\pi^- \to K^-} = \frac{2R_u}{1+R_u} \to 2R_u \qquad (3.10)$$

both in the data and in the model for large x. The two ratios are related by line reversal and charge conjugation. They would become equal in the model whenever the favoured and unfavoured kaon spectra became proportional to the respective pion spectra, i.e.

$$D_u^{K^-} \approx D_d^{K^+} \approx D_d^{K^-} \approx \lambda D_u^{\pi^-}$$

$$D_u^{K^+} \approx \lambda D_u^{\pi^+}$$

and furthermore, if $\alpha = \beta = 0.5$. That is clearly only approximately true.

In Fig. 11c we look at the ratios of unfavoured transitions with K and π beams. Both ratios shown behave in a similar way and a strong suppression in kaon beams is observed at large x. This is only partly reproduced by the model for the kaon and fails for the pion ratio where we obtain

$$\frac{K^- \to \pi^+}{\pi^- \to \pi^+} = \alpha + \beta D_s^{\pi^+} / D_u^{\pi^-} \approx 1 \qquad (3.11)$$

Here the equality $D_s^{\pi+} \approx D_u^{\pi^-}$ (eq. 3.4) is a special property of the Field Feynman model not yet checked experimentally. One should also remark that (3.11) is a ratio of small rates with large errors for large x. The discrepancy at large $x > 0.6$ is related to the shoulder in $\pi^- \to \pi^+$. If this is due to diffractive A_1 production, one may expect a corresponding effect for $K^- \to \pi^+$ from $K^- \to Q^-$ ($Q^- \to K^{*o}\pi^-$, $K^{*o} \to K^-\pi^+$ with branching ratio 2/3), though in a smaller x range because of the unequal mass kinematics. Therefore diffraction is expected to increase the above ratio above 1 at smaller x and below one only at larger x, contrary to the data. One way out would be to take $D_s^{\pi+} < D_u^{\pi^-}$, different from the Field Feynman model.

The other ratio in Fig. 11c can be expressed as

$$\frac{K^- \to K^+}{\pi^- \to K^+} \approx 2/(1 + D_d^{K^+} / D_u^{K^-}) \qquad (3.12)$$

independent of α, using eq. (3.4b) and the agreement with the prediction is satisfactory, taking into account the uncertainty in the D-functions involved.

Estimate of the λ-parameter

Looking at the overall success of the model we may estimate the s quark suppression factor λ from K/π ratios in Fig. 9b. As the ratios involving different beams are not reproduced that well (Figs. 11a, c) and reflect the complication of different quarks in the K^-, the most direct way is to look at the ratio

$$\frac{\pi^- \to K^-}{\pi^- \to \pi^o} = \frac{D_u^{K^+}\,(1 + D_d^{K^-} / D_u^{K^+})}{D_u^{\pi^+}\,(1 + D_u^{\pi^-} / D_u^{\pi^+})} \approx \frac{D_u^{K^+}}{D_u^{\pi^+}} \qquad (3.13)$$

where the last equation holds within ~ 10% in the model, and this ratio is a direct measure of λ for large x. Our results in Fig. 9b yield the value $\lambda = 0.2$. This is smaller than the value $\lambda = 0.3$ suggested within the above statistical model (1) using all three ratios in Fig. 9b, but it agrees nicely with the value $\lambda = 0.2$ found in νp scattering [26].

3.2.2b Dual Parton Model

After the original success of this simple fragmentation model [7] further models have been proposed in which the original valence quarks are distributed over the entire range from $x = 0$ to $x = 1$. We discuss here only the model proposed by the groups at Orsay [8] and Saclay [9], who investigated the correspondence between the quark fragmentation picture and a certain dual Regge model and still employ the quark fragmentation functions.

The valence quarks a and b in the beam particle acquire the distributions $U_a(x)$ and $U_b(x) = U_a(1-x)$ and, after fragmentation, yield two overlapping chains of hadrons. The behaviour of $U_a(x)$ near $x = 0$ (and also $U_b(x)$ near $x = 1$) is determined by the intercept $\alpha_{a\bar{a}}$ of the leading Regge trajectory $\alpha_{a\bar{a}}(t)$ at $t = 0$ which contains the hadron states $(a\bar{a})$, and the model yields $U_a(x) \sim x^{-\alpha_{a\bar{a}}}$ near $x = 0$. The distribution $U_a(x)$ may then be chosen as [9]

$$U_a(x) = \left(\frac{1-x}{x}\right)^{\alpha_{a\bar{a}}} \Theta(\tfrac{1}{2} - x) + \left(\frac{x}{1-x}\right)^{\alpha_{b\bar{b}}} \Theta(x - \tfrac{1}{2}) \qquad (3.14)$$

and the inclusive spectrum for the transition $H(a,b) \to H'$ follows by convolution with the appropriate decay function $D_q^{H'}$

$$\pi\rho^{H\to H'}(x) = \int_0^1 dy\, U_a(y) \left[\frac{x}{y} D_a^{H'}\left(\frac{x}{y}\right) \Theta(y-x) + \frac{x}{1-y} D_b^{H'}\left(\frac{x}{1-y}\right) \Theta(1-y-x)\right] \qquad (3.15)$$

$$/ \int_0^1 dy\, U_a(y)$$

With $\alpha_{u\bar{u}} = \alpha_{d\bar{d}} = \tfrac{1}{2}$ the distribution $U_a(x)$ is peaked at $x = 0$ and $x = 1$ for the pion beam, whereas in the kaon beam, choosing $\alpha_{s\bar{s}} = 0$ the s quark distribution is again peaked at $x = 1$ but is flat near $x = 0$. Therefore for large x the s-quark fragmentation is enhanced over the $\bar{u}$ quark fragmentation.

In Fig. 12 we show again our data on π production (disregarding $\pi^- \to \pi^\pm$ with their presumably large diffractive contributions) together with the prediction (solid curve) from the previous model (2a) which corresponds to $U(x) = \delta(x) + \delta(1-x)$, and with the prediction (broken line) from the convolution $U \otimes D$ with eqs. (3.14, 3.15). It appears that in most cases the spectra resulting from the convolution become somewhat too steep and fall below the data.

To study the sensitivity to the input quark decay functions we also show in Fig. 12 the $D_u^{\pi\pm}$ functions as determined from νp scattering [27]. The agreement between the data and corresponding Field Feyman model curves (solid lines) is satisfactory. Furthermore our data do not fall significantly steeper with x than the corresponding neutrino data as would be expected from the convolution (3.15), but the spectra agree within a band of ~ 2 standard deviations. One should keep in mind though the uncertainty coming from relations 3.4a and 3.5 used here and from possible diffraction dissociation.

It is instructive to derive an approximate expression for the suppression of $\rho(x)$ with respect to the input decay function D_{inp} at large x (say $x \geq 0.9$). Here we may approximate eq. (3.15) by

$$\pi\rho^{H\to H'}(x) \approx [\, D_a^{H'}(x') \frac{(1-x)^{1-\alpha_{b\bar{b}}}}{1-\alpha_{b\bar{b}}} + D_b^{H'}(x'') \frac{(1-x)^{1-\alpha_{a\bar{a}}}}{1-\alpha_{a\bar{a}}} \,] / \int U dy \quad (3.16)$$

with some appropriate values $x < x', x'' < 1$.

In case of $\pi^- \to \pi^o$ we obtain with $\int U dy = 2.38$

$$\pi\rho^{\pi^-\to\pi^o}(x)/D^{\pi^o}(x) \approx 1.68(1-x)^{1/2} \quad (3.17)$$

so at x = 0.9 (0.95) the suppression by convolution is 0.53 (0.38). In case of $K^- \to \pi^-, \pi^o$ the suppression is stronger as the dominant source of pions in the input function is the fast $\bar{u}$ quark which is now suppressed already in the $U_s(x)$ distribution. With $\int U dy = 1.69$ and $D_{inp} \approx 0.4\, D_u^{\pi+}$ we find

$$\pi\rho^{K^-\to\pi^-}(x)/D_{inp}(x) \approx 1.48\,[(1-x) + 2D_s^{\pi}(x')(1-x)^{1/2}/D_u^{\pi+}(x'')] \quad (3.18)$$

where the first term with the leading $\bar{u} \to \pi^-$ fragmentation vanishes stronger than in (3.17) and we find at x = 0.9 (0.95) the stronger suppression factor of 0.25 (0.11).

It appears that the fragmentation into pions is rather well described by a superposition of two quark jets carrying the full momentum. In any fragmentation model using the standard quark decay function D_q^H a distribution U(x) sharply peaked at x = 0 and x = 1 (stronger than in 3.14) is required to describe the data.

3.2.3 Recombination Model

Whereas in the fragmentation models the constituent valence quarks of the beam particle carry together the full momentum and then fragment, in the recombination models one starts from the initial distribution $p_H(x)$ of partons of type p (valence quarks, sea quarks and gluons) in the beam particle H, which are inferred from measurements of deep inelastic scattering. The idea is that the valence quark distribution is not strongly altered by the collision [11]. Fast mesons H′ are produced after recombination of a fast valence quark q with a slow sea quark and one expects then the approximate proportionality

$$\frac{1}{\sigma}\frac{d\sigma^{H\to H'}}{dx} \sim q_H(x) \tag{3.19}$$

between the distribution of valence quark q and the meson H′ which carries it [10,12]. Further developments have led to models involving more detailed parametrisations [13] or incorporating the momentum transfer Q^2 dependence of the structure functions [28].

Whereas detailed measurements of the various parton distributions inside the nucleon became available from deep inelastic scattering, much less is known about such distributions inside the meson, where the only source of information by now is lepton pair production. In fact, the recombination model [13] has been used to derive such distributions from hadronic collisions [29].

Here we restrict ourselves to a test of (3.19) by comparing the distributions of u quarks in the pion and kaon with our distributions of π^o's in the pion and kaon fragmentation region. With (3.19) one expects for large x

$$\frac{\bar{u}_{K^-}(x)}{\bar{u}_{\pi^-}(x)} \to \frac{\rho^{K^-\to\pi^o}(x)}{\rho^{\pi^-\to\pi^o}(x)/2} \tag{3.20}$$

where the factor 1/2 takes into account that both valence quarks in the π^- may yield a fast π^o. On the other hand, at small x the l.h.s. is expected to approach ~ 1, the r.h.s. to approach 2.

In Fig. 13 we compare our data with the structure function ratio derived from lepton pair production [30]. Both data sets approach each other at large x and reflect the suppression of the $\bar{u}$ quark at large x in the K^- with respect to the π^-. This behaviour of that ratio at large x may be compared to the prediction from the statistical model to be one (Fig. 9) and to be $2\alpha = 0.8$ in the fragmentation model (Fig. 11). For $x \leqq 0.7$ the relation 3.20 gets violated and this may be interpreted as onset of sea-sea recombination processes.

3.2.4 Counting Rules

Following previous work on counting rules [14], Gunion [15] has argued that the production of particles with large x requires certain internal gluons to go far off shell, so that perturbative QCD can be applied. He derives a power behaviour $(1-x)^n$ for the inclusive distribution of hadrons near $x = 1$, where the power n depends on the quantum numbers of the incoming and outgoing particles. For our spectra in the classes (VS) and (SS) one obtains the leading contributions from the diagrams in Fig. 14 with powers $n = 1$ and $n = 3$ respectively.

The predicted shapes are compared to our data in Fig. 8. In class VS the $K^- \to \pi^o$ data follow closely the curve whereas the other spectra appear to fall more gently rather consistent with an exponential decrease for $x > 0.6$. In class SS the $K^- \to \pi^+$ data follow beautifully the predicted shape essentially over the full x range explored, whereas the K^+ spectra are slightly flatter than expected. Again the exceptional $\pi^- \to \pi^+$ spectrum does not fit into the overall view.

It should be noted that in this calculation the actual shape of the x distribution is predicted from the quark structure of the process whereas in model 1 only the ordering of spectra is given and in models 2 and 3 the observed spectra are related to other measurements without predicting their shape. On the other hand there is the ambiguity that several diagrams may usually contribute to one process and the relative normalisation is not known. For example, the fast particles in class SS are produced by a simultaneous emission of gluons from both valence quarks (Fig. 14); if one would take instead a diagram where both gluons come from the same valence quark, corresponding to a conventional quark jet model, one would obtain as leading power $n = 4$ inconsistent with all spectra. A compilation of power fits to various x spectra can be found elsewhere [3].

4. INCLUSIVE p_T DISTRIBUTION

4.1 General Characteristics of p_T Spectra

Our results on the p_T dependence of the invariant cross-sections for fixed x are presented in Figs. 15-17. All spectra show an exponential decrease for large p_T and a depletion at small p_T which is stronger for kaons than for pions, and furthermore becomes less pronounced with increasing x. The shape may also vary slightly from one reaction to another.

Our data are grossly incompatible with a simple exponential behaviour in any of the variables p_T, p_T^2, transverse mass $m_T = (m^2 + p_T^2)^{1/2}$ or four momentum transfer $t = (p_i - p_f)^2$ between beam and secondary particle. Good fits to all data could be obtained by an expression containing two parameters A and M.

$$E \frac{d\sigma}{d^3p} \sim \exp(- A \sqrt{p_T^2 + M^2}) \qquad (4.1)$$

which behaves like a Gaussian for small $p_T \ll M$ and like an exponential for large $p_T \gg M$ (see Figs. 15-17).

The variation of A and M with x can be seen in Fig. 18 for the various transitions. Unfortunately the results on A and M from the χ^2 fit are positively correlated such that both values could be raised or lowered at the same time by more than expected from the errors in the figure*). The following trend can be seen in Fig. 18: the mass parameter M decreases from M ~ 1 GeV at x ~ 0.2 to M ~ 0.2 GeV at x ~ 0.9. This means at small x the Gaussian shape and at high x the exponential shape in p_T is more dominant, though neither form describes the full p_T range explored here.

We also show in Fig. 18 the average p_T values. For pions they fall in general within a band of width ± 10% and the same is true for the kaons. However, at large $x \geq 0.8$, the diffractively produced particles (VV transitions) acquire larger p_T than the particles with exotic SS transitions, whereas the VS transitions fall rather in between.

---

*) The errors refer to the diagonal errors calculated from the second derivative of the χ^2 function at minimum.

Finally we compare our data with the results from other experiments. The overall shape of p_T spectra for charged particles agrees well with the results by Brenner et al. [16] in the overlapping p_T range (see Fig. 19). In particular, the change from a Gaussian to an exponential shape with increasing x in this p_T range has been observed first by this group. The difference in normalisation at small x was already noted in Section 3. High statistics data on inclusive π^0 production have been obtained by a CALTECH-LBL collaboration for $x > 0.5$ in $\pi^- p$ and for $x > 0.5$, $t < 0$ in $K^- p$ collisions [17]. The agreement with our measurements is satisfactory (Fig. 19).

4.2 Quantum Number Dependence and Leading Particles

In Fig. 20a-c we show for $0.6 < x < 0.8$ various ratios of particles with the same mass but different quark composition and no significant dependence on p_T is observed. On the other hand the K/π ratios do increase with p_T. The three ratios in Fig. 20d for the same beam particles are a measure of the quark suppression factor λ in the fragmentation models of Section 3. They show an increase by about a factor 2 as also seen in neutrino scattering [26].

It is interesting to note that the cross-section for $K^- \to K^-$ is suppressed with respect to $\pi^- \to \pi^-$ at small p_T but they approach each other at $p_T \geq 1$ GeV (see Fig. 15). One may suppose that this suppression of the leading K^- at small p_T is finally responsible for the smaller $K^- p$ total cross-section, as the integral over the leading particle spectrum $d\sigma/dx$ should be proportional to the total (inelastic) cross-section σ_{in}. A more precise test of this idea would be possible, for example, in an experiment with π^+ and K^+ beams by comparing the total charge distribution $d\sigma(a \to h^+)/dp_T - d\sigma(a \to h^-)/dp_T$ integrated over all x which is normalised to σ_{in}, for both reactions, and check whether the difference comes only from small p_T.

4.3 Transition to the Large p_T Region

The lack of quantum number dependence of p_T spectra has triggered a more detailed analysis of the particular ratio $(\pi^- \to \pi^+)/(\pi^- \to \pi^-)$ which compares an exotic with a leading particle transition, where also data from large p_T experiments are available. If the final π^- in the transition $\pi^- \to \pi^-$ would carry both incoming valence quarks, its p_T dependence is expected to be steeper than that of the π^+ which can be produced by single quark fragmentation, using the argument that a composite object is more difficult to scatter than an elementary object (see, for example, ref. [14]).

To investigate this question over a large kinematical region we plot in Fig. 21 our data on the π^+/π^- ratio for fixed $x_R = 2E_{CM}/\sqrt{s}$ as a function of the CM scattering angle Θ_{CM}. We also included here our data on the ratio h^+/h^- using all charged particles detected in the larger aperture of Arm I + II, using our full data sample (see Section 2). It is known from previous experiments that such particle ratios do not show any significant energy dependence [31] as is also predicted in theoretical models*). We therefore include in Fig. 21 also the measurements at Fermilab at p_{lab} = 200 GeV/c at larger angles [32].

At $\Theta_{CM} \approx 90°$ the π^+/π^- ratio tends to approach 1 and the influence of the negative and positive charge of beam and target particles compensate each other. Moving towards smaller angles Θ_{CM} for fixed x_R we observe a decrease which rather smoothly connects to our measurements, and the main variation occurs in the angular range $60° < \Theta_{CM} < 90°$. The h^+/h^- ratio in K^-p collisions (Fig. 21) shows a similar behaviour. It is also interesting to note that the predictions from the QCD model by Field [35] come close to the measurements (see Fig. 21). This model is based on quark quark scattering with subsequent quark fragmentation [34] and has no separate leading particle effect included. The results from K^- fragmentation in Fig. 21 on h^+/h^- look rather similar.

It appears that the leading mesons do not play any special role but they can be looked at as coming primarily from quark fragmentation. This is different from the situation in pp collisions, where on one hand the particle ratios π^+/π^- and K^+/K^- are almost independent of the angle Θ_{CM} for fixed x_R [36,12], whereas the ratio p/p is strongly angular dependent. This difference could be understood if all mesons and the $\bar{p}$ came from single quark fragmentation for either meson or proton beams, whereas the $p \to p$ transition involves a diquark fragmentation with a steeper p_T dependence.

---

*) The nonscaling p_T^n factors in $Ed\sigma/d^3p \sim p_T^n f(x_R,\Theta)$ are the same for π^+ and π^- (see for example, refs. [33] or [34]).

5. TWO PARTICLE CORRELATIONS

5.1 Two Representative Models of the Recombination and Fragmentation Type

It is conceivable that both the recombination and the fragmentation model can be formulated to yield equivalent observable results though the language is quite different (constituent quark fragmentation vs. current quark recombination); indeed the predictions on single inclusive spectra are very similar [37,3]. It appears however that the originally proposed ideas lead in fact to different predictions on two particle correlations.

The valence quarks in the incoming meson will be carried in general by two different final hadrons ("valence hadrons") with momenta x_1 and x_2. In the fragmentation model one quark is held back (say $x_2 \leqq 0.1$) and therefore also the valence quark fragmenting from it is held back at small $x < x_2$ [7-9]. On the other hand, in the recombination model, when the initial valence quarks "fly through" [11,12], both valence quarks may acquire large x in the fragmentation region (say $x > 0.2$).

This situation is realised for example in the model by Takasugi and Tata [38] following earlier work [39] with Kuti-Weisskopf multiquark structure functions [40]. There are also models which appear to fall in between, namely the later version of the Lund-Fragmentation model [41], where a single long chain of hadrons is initiated by one of the valence quarks at $x = 1$ as before, but the second valence quark in the meson is not necessarily carried by a slow valence hadron; also the quark cascade model by Fukuda et al. [42] combines elements of fragmentation and recombination.

In view of this variety of possibilities it is interesting to investigate experimentally how the two valence hadrons are distributed. For this purpose we trigger on a fast negative hadron h_1^- at momentum x_1 which may select one of the initial valence quarks and then study the distribution of the remaining positive and negative particles h_2^+ and h_2^- in momentum $x_2 < 1-x_1$ or rather in the reduced scaling variable $x' = x_2/(1-x_1)$. This should give us information on the distribution of the second valence hadron. Instead of implementing any of the above rather complex models on the computer, we have constructed two rather simple representative versions of the fragmentation model ("held back quark") and the recombination model ("flying through quarks") which are in rough agreement with single charged particle spectra and therefore should be sufficient for a quantitative estimate of the differences to be expected in both types of models.

Model I ("held back quark")

In our case of a π^- beam the fast negative trigger particle will be most likely the first fragment of the initial $\bar{u}$ or d valence quark at $x \approx 1$ leaving behind a u, $\bar{d}$ or $\bar{s}$ quark. These positively charged quarks will initiate a new cascade of hadrons and we expect then

$$h_2^+/h_2^- \gg 1 \quad \text{for } x' \to 1 \tag{5.1}$$

To estimate this effect we consider a simple chain cascade model as in [24] with $\lambda = 0.2$. Furthermore, we restrict to pseudoscalar mesons and neglect transverse momentum and η,η' decays. Each quark in the chain fragments into a hadron according to the momentum sharing function $f(x) = 2(1-x)$. This yields inclusive distributions of h^+ and h^- which do not deviate by more than ~ 30% from the distributions obtained in [24]. If $f(x)$ were replaced by $f(x) = 1$ the ratio h^+/h^-, which is of primary importance here, would still remain essentially unaltered.

Model II ("flying through quarks")

After removing the fast negative trigger particle, the second particle may come either from the same quark jet or from the second (negatively charged) valence quark. In the first case this second particle will be mostly positive for $x' \to 1$, and in the second case mostly negative. Therefore one expects

$$h_2^+/h_2^- \approx 1 \quad \text{for } x' \to 1 \tag{5.2}$$

To represent this situation we give the initial two valence quarks a flat x distribution $U(x) = 1$ with $x_1+x_2 = 1$, and then each quark gives rise to a hadron cascade as described above for Model I but with $f(x) = 1$ instead. We know already from Section 3 that a fragmentation model with the standard quark decay functions (as in model I) requires the initial valence quark distribution U(x) to be sharply peaked at $x = 0$ and $x = 1$. In order to incorporate $U(x) = 1$ within a cascade model, we therefore have to make f(x) less steep in order to reproduce the single inclusive spectra. Then f(x) in this soft process becomes different from the f(x) usually defined in hard processes.

5.2 Comparison with Data

In Fig. 22 we show first the distributions in x' of h_2^+ and h_2^- after a negative particle has been removed at x_1 for three intervals of x_1. For this study involving only charged particles we use our full data sample. The x variables refer again to the lab frame. We have included all tracks accepted within the larger aperture of our apparatus but restricting to $p_T < 10x$ which correspond to the forward hemisphere in the CM frame (for $p_T \gg$ mass). Correlations as in Fig. 22 have been studied already for other types of particles [43-46] whereby an approximate scaling of spectra in x' for different x_1 has been observed, as it is also expected from certain recombination models [38]. Our more precise data show however that scaling is broken in a way which is familiar from deep inelastic collisions, namely, with increasing available energy (decreasing x_1) the spectra in general rise at small x' and decrease at large x'. This phenomenon has also been observed in a similar correlation experiment at the ISR [47].

Now we turn to the main result of this section (Fig. 23) which shows the ratio of h_2^+/h_2^- after a negative particle has been removed (these are the ratios of the spectra in Fig. 22). The curves represent our model calculations which are in agreement with the expectations (5.1) and (5.2) from our previous qualitative arguments. The single chain model with a "held back" quark leads to a large ratio of h_2^+/h_2^-. Though the data are consistently positive around $h_2^+/h_2^- \sim 1.4$ they do not follow the strong increase predicted from the model which yields $h_2^+/h_2^- > 4$ for $x' > 0.8$. For comparison we also show the ratio h^+/h^- derived from the Field Feynman model [24] for a superposition of a u and $\bar{d}$ quark jet which is left in Model 1 after the π^- has been removed. The result is similar to our simple model calculation above. On the other hand, the data are always above the prediction from the second model with "flying through" quarks though the data tend to decrease towards large x' rather than to rise as would be expected from the first model.

We have also done a calculation using the two chain models [8,9] where the valence quarks have an initial distribution U(x) as in eq. 3.14 and fragment as in Model 1 above. This model, which has been seen already to yield too steep single inclusive spectra, is found to be roughly consistent with our data for small x_1 and x' in Fig. 23, but the ratio h_2^+/h_2^- again rises rapidly for $x_1 > 0.4$ and $x' > 0.3$ where it tends to approach Model 1.

We conclude from Fig. 23 that the forward fragmentation cannot be described by a single chain with one valence hadron, whereas the second valence hadron is held back at small $x < 0.1$. Instead the second valence hadron has to acquire a large fraction of momentum x with a rate which is smaller than assumed in our Model 2, but still sufficient to bring the h_2^+/h_2^- ratio down to the smaller values 1.0 . . . 1.4 observed for large x'.

A similar conclusion has also been drawn from a study of charge and energy distributions [48] where the ratio $\Delta Q/\Delta E$ was found to exceed the value 1/2 expected for a single quark jet but to be consistent with expectations from a broader momentum distribution of the initial valence quarks [49,50].

There are some models [38,41,42] which appear to yield final states with two fast valence hadrons and it would be interesting to work out a detaild comparison. Here we only emphasise that Fukuda et al. [42] have considered correlations between charged particles $\pi^- \to \pi^{ch}(x_1)\ \pi^{ch}(x')$ as in our Fig. 22 but without distinguishing h^+ and h^-. To a good approximation we can compare this to $\pi^- \to h^-(x_1)\ h^{ch}(x')$ where $h^{ch}(x') = h^+(x')+h^-(x')$ is the respective sum of spectra in Fig. 22. The result of their calculation for $x_1 \sim 0.5$ comes rather close to our data in shape and normalisation (Fig. 24). The model also reproduces the trend of scale breaking in our data as shown by the second curve for $x_1 \sim 0.1$.

5.2 Influence of Diffraction Dissociation

One could suspect that the small ratio h_2^+/h_2^- for $x' \to 1$ is due to inelastic diffraction dissociation. Indeed, taking as an example the production and decay of $A_1^- \to \pi^+\pi^-\pi^-$ our trigger would remove a π^- and leave behind a π^+ and π^-, hence $h_2^+/h_2^- \approx 1$. However one should note that single diffraction dissociation occurs only at a rate of 10–15% of the inelastic cross-section and can therefore hardly be responsible for the discrepancy between data and Model 1 seen in Fig. 23 which occurs for all x_1 and $x' \geq 0.2$.

To arrive at a more definite conclusion we have repeated the above analysis but requiring a large invariant mass of the particle pairs $M(h_1^-, h_2^\pm) > 1.2$ GeV. This will remove the events with low mass diffraction dissociation like A_1. The results for h_2^+/h_2^- are shown in Fig. 25 and does not show any significant change (except for 2 data points at $x_1 \sim 0.5$, $0.7 < x' < 0.9$). The same has also been done with the larger cut $M(h_1^-, h_2^\pm) > 2$ GeV with a similar result. We therefore conclude that low mass diffraction dissociation cannot explain the discrepancy between our data and Model 1.

Dependence on the Trigger p_T

We have also studied how the ratio h_2^+/h_2^- depends on the p_T of the trigger particle h_1^-. More specifically we have determined for a given x_1 and p_T of h_1^- the ratio h_2^+/h_2^- where both particles have $x' > 0.5$. If the p_T becomes large, such that hard scattering models can be applied (for example [34]), we would expect that the h_1^- carries one valence quark, whereas the other valence quark with negative charge is flying through and is contained in the "spectator jet", therefore $h_2^+/h_2^- < 1$ holds for the remaining low p_T particles. This is indeed observed (Fig. 26) for $0.2 < x_1 < 0.4$ and for $p_T \geq 1$ GeV/c (corresponding to $\Theta_{CM} \approx 30° \ldots 50°$). For $x_1 > 0.4$ that ratio is close to 1 for small p_T and appears to level off at some value around 1.6, but is still far away from the value ~ 3.5 which would be expected in Model 1 above for the ratio h^+/h^- with $x' > 0.5$. Therefore a single quark jet is also not realised in an intermediate p_T range of the trigger particle, but a considerable contribution from the second valence quark to the remaining particles h_2 is necessary. So we observe here a smooth transition from the small p_T to the large p_T region where the second quark initiates the spectator jet.

6 SUMMARY, COMMENTS AND CONCLUSIONS

We have studied forward particle production using a large acceptance spectrometer with the ability to identify charged and neutral particles. Inclusive x and p_T spectra for 10 different transitions in the range of $x > 0.2$ and $p_T < 1.5$ GeV/c and also data on charged particle correlations have been presented. The data have been compared with various models which attempt to explain soft hadron hadron collisions by the interaction of their quark constituents. We want to summarise this study as follows.

(1) The statistical Quark model [6] gives a good classification of x-spectra in terms of through going valence quarks though there are deviations from the predicted particle ratios. For example the ratio $(K^- \to \pi^0)/(\pi^- \to \pi^0)$ does not approach the predicted value 1/2 but deviates by ± 40% (Fig. 9).

(2) Jet universality and fragmentation model. Our single inclusive x-spectra are in remarkable agreement with the simple ansatz [7] which represents the non diffractive low p_T jets as an appropriate superposition of quark jets. This comparison is limited by the incomplete knowledge of quark fragmentation functions where we have taken the Field Feynman jet parametrisation. Some discrepancies are resolved by more recent measurements, in particular the quark suppression factor λ is found here as well as in νp scattering to be $\lambda \approx 0.2$ rather than $\lambda = 0.5$ in that model. The other uncertainty is from diffraction dissociation which is apparently large for $\pi^- \to \pi^{\pm}$, $K^- \to K^-$ at large x. Otherwise, taking into account $\lambda \approx 0.2$ the agreement of the model with our data is typically better than 30% (Fig. 10). In order to test jet universality further and to higher precision, one would need an updated quark jet parametrisation and some supplementary model for diffraction dissociation.

(3) Dual chain fragmentation model [8,9]. Whereas this model provides a theoretical justification for the simple ansatz of (2), we encounter two difficulties in the comparison to our data: (a) the convolution of the initial valence quark distribution U(x) (eq. 3.14) with Field Feynman fragmentation functions yields single inclusive spectra which fall too steeply at large x (Fig. 12) and (b) as one valence quark is held back at small x a large ratio h_2^+/h_2^- for a h_1^- trigger is expected but not observed in our correlation data (Fig. 23). We have argued that this discrepancy is not primarily due to diffraction dissociation. On the other hand, one has to check whether the calculation within the quark cascade model is really in agreement with appropriate measurements on quark jets in hard processes as tacitly assumed here. If so, the correlation measurements would discriminate between jets in soft and hard collisions as jets carrying two or one fast valence hadrons respectively. Then the phenomenological concept of "jet universality" would not apply to such more detailed properties of jets.

(4) Recombination models. Only one new test which related directly the quark distributions in pions and kaons to appropriate inclusive meson spectra [10,12] was possible (Fig. 13) as not much is known about meson structure functions. A more detailed comparison would require models for these functions (see e.g. ref. [38]). The deviation of our correlation data from the "held back" quark model could be interpreted as evidence for the second valence quark to be carried by a fast hadron. This is in qualitative agreement with the recombination model where the initial valence quarks fly through during the interaction, though our (rather simple) model estimate here gave too strong an effect. It would be interesting to see to what extent more detailed recombination models [38] or other models with two fast valence hadrons [41,42] can explain the data.

(5) Counting rules [15]. We find reasonable agreement between our x-spectra and the shapes predicted from diagrams corresponding to the leading power in (1-x).

(6) Phenomenology of p_T distributions. The p_T distributions vary with x in a similar way for all particles, only for $x > 0.8$ they become very different depending on the quantum numbers. In particular the leading particles ($\pi^- \rightarrow \pi^-$) have a p_T distribution very similar to the non leading particles and the π^+/π^- ratio does not vary much for $\Theta_{CM} < 60°$ where it joins smoothly to large p_T measurements and model expectations based on quark quark scattering with subsequent fragmentation (Fig. 21). The same is also true for our correlation measurements.

Conclusions. The study of our data has revealed support for various ideas related to low p_T hadron hadron collisions. Particularly impressive is the confirmation of jet universality in comparing inclusive spectra for soft and hard processes. However a simple model of the collision describing the fate of both valence quarks, comparable to the parton models for hard scattering processes, could not yet be presented. Hopefully a further detailed comparison of soft and hard processes including correlations will serve this goal.

REFERENCES

[1] E.M. Levin, L.L. Frankfurt, JETP Lett. 2, (1965) 65;
H.J. Lipkin, F. Scheck, Phys. Rev. Lett. 16 (1966) 71.

[2] P.D.B. Collins, A.D. Martin, Rep. Prog. Phys. 45 (1982) 335.

[3] K. Fialkowski, W. Kittel, Rep. Prog. Phys. 46 (1983) 1283.

[4] Proc. Europhysics Study Conf. on Partons in Soft Hadronic Processes, Erice, Ed. R.T. Van de Walle, World Scientific Singapore (1981).

[5] H. Satz, Phys. Lett. 25B (1967) 220.

[6] V.V. Anisovich, V.M. Shekhter, Nucl. Phys. B55 (1973) 455.

[7] B. Anderson, G. Gustafson, C. Peterson, Phys. Lett. 71B (1977) 337, and 69B (1977) 221.

[8] A. Capella, V. Sukhatme, C.I. Tan, J. Tran Thanh Van, Phys. Lett. 81B (1979) 68;
A. Capella, V. Sukhatme, J. Tran Thanh Van, Z. Phys. C3 (1980) 329.

[9] G. Cohen-Tannoudji, A. El-Hassouni, J. Kalinowski, O. Napoly, R. Peschanski, Phys. Rev. D21 (1980) 2689; Phys. Rev. D19 (1979) 3397.

[10] H. Goldberg, Nucl. Phys. B44 (1972) 149.

[11] S. Pokorski, L. Van Hove, Nucl. Phys. B86 (1975) 243.

[12] W. Ochs, Nucl. Phys. B118 (1977) 397.

[13] K.P. Das, R.C. Hwa, Phys. Lett. 68B (1977) 459.

[14] R. Blankenbecler, S.J. Brodsky, Phys. Rev. D10 (1974) 2973.

[15] J.F. Gunion, Phys. Lett. 88B (1979) 150.

[16] A.E. Brenner et al., Phys. Rev. D26 (1982) 1497.

[17] A.V. Barnes et al., Nucl. Phys. B145 (1978) 45;
R.G. Kennett et al., Nucl. Phys. B177 (1981) 1.

[18] G. Ascoli et al., MPI report MPI-PAE/Exp. El. 77 (1979);
C. Daum et al., Z. Phys. C8 (1981) 95.

[19] C. Daum et al., Nucl. Phys. B182 (1981) 269;
C. Daum et al., Nucl. Phys. B187 (1981) 1.

[20] E.O. Abdrakhmanov et al., Nucl. Phys. B72 (1974) 189.

[21] J. Whitmore et al., Phys. Rev. D16 (1977) 3137.

[22] G.J. Bobbink, Thesis, University of Utrecht (1981);
G.J. Bobbink et al., Nucl. Phys. B204 (1982) 173.

[23] H. Grässler et al., Nucl. Phys. B132 (1978) 1.

[24] R.D. Field, R.P. Feynman, Nucl. Phys. B136 (1978) 1.

[25] P.K. Malhotra, R. Orava, Z. Phys. C17 (1983) 85.

[26] G.T. Jones et al., MPI report MPI-PAE/Exp. El. 141 (1984), and L. Deck, private communication.

[27] P. Allen et al., Nucl. Phys. B214 (1983) 369.

[28] R.C. Hwa, Phys. Rev. D22 (1980) 759.

[29] N.N. Biswas et al., Phys. Rev. D19 (1979) 1960;
W. Aitkenhead et al., Phys. Rev. Lett. 45 (1980) 157.

[30] J. Badier et al., Phys. Lett. 93B (1980) 354.

[31] D. Antreasyan et al., Phys. Rev. Lett. 38 (1977) 112.

[32] H.J. Frisch et al., Phys. Rev. Lett. 44 (1980) 511.

[33] R. Blankenbecler, S.J. Brodsky and J.F. Gunion, Phys. Lett. 39B (1972) 649.

[34] R. Feynman, R.D. Field, G. Fox, Nucl. Phys. B128 (1977) 1.

[35] R.D. Field, Phys. Rev. D27 (1983) 546.

[36] J.R. Johnson et al., Phys. Rev. D17 (1978) 1292.

[37] A. El Hassouni, O. Napoly, Phys. Rev. D23 (1981) 193.

[38] E. Takasugi, X. Tata, C.B. Chiu, R. Kaul, Phys. Rev. D20 (1979) 211;
E. Takasugi, X. Tata, Phys. Rev. D26 (1982) 120.

[39] T. De Grand, H. Miettinen, Phys. Rev. Lett. 40 (1978) 612.

[40] J. Kuti, V. Weisskopf, Phys. Rev. D4 (1971) 3418.

[41] B. Anderson, G. Gustafson, I. Holgersson, O. Mansson, Nucl. Phys. B178 (1980) 242.

[42] H. Fukuda, Y. Ishihara, C. Iso, Prog. Theor. Phys. 65 (1981) 961.

[43] E. Lehmann et al., Phys. Rev. D18 (1978) 3353.

[44] E.A. De Wolf et al., Z. Phys. C8 (1981) 189.

[45] H. Abramowicz et al., Univ. of Cracow preprint (1979).

[46] W. Lockmann et al., Phys. Rev. Lett. 41 (1978) 680.

[47] M. Basile et al., Phys. Lett. 92B (1980) 367.

[48] I.V. Ajinenko et al., Z. Phys. C16 (1983) 291.

[49] W. Ochs, T. Shimada, Z. Phys. C4 (1980) 141.

[50] B. Andersson, G. Gustafson, Phys. Lett. 84B (1979) 483.

Figure Captions

Fig. 1 Plan view of the ACCMOR spectrometer showing the target (T), the magnets (M1, M2), the Cerenkov counters (C1, C2), the γ-calorimeter, and 4 sets of wire chambers (arm I-IV). The trigger was defined by the useful beam (UB) and beam Cerenkov counters (BC) in anticoincidence with the D counter.

Fig. 2 Geometrical acceptance as a function of x and p_T for charged particles (a) with Cerenkov identification (smaller aperture) and (b) without (larger aperture). The acceptance rises almost linearly from the lines A = 0% to A = 100%. For negative particles the acceptance drops again to zero towards x = 1 and p_T = 0 GeV/c.

Fig. 3 Efficiencies of Cerenkov counters determined from our data using eq. 2.3 (triangles) and from another experiment [19] using the same experimental setup.

Fig. 4 (a) two photon mass spectrum showing the π^o peak,
(b)-(d) the flat decay photon spectrum for various intervals of the π^o energy E_{π^o}. The drop below the dashed line is due to the finite width of the E_{π^o} interval.

Fig. 5 Single inclusive cross-sections from this experiment. Systematic errors are included but not the overall normalisation uncertainty of 8%.

Fig. 6 Relations between CM and lab quantities. Here $x_T = 2p_T/\sqrt{s}$ and $x_R = (x_{CM}^2 + x_T^2)^{1/2}$.

Fig. 7 Comparison of some representative x spectra from our experiment (full data points) with the results from refs. [16,20] (open points).

Fig. 8 Single inclusive spectra as in Fig. 5 but normalised to the inelastic total cross-section σ_{in}, classified according to the number of valence quarks contained in the final particle. The appropriately scaled spectra are expected in the statistical quark model [6] to occur with the relative weights as indicated. Also shown are the shapes $(1-x)^n$ predicted by counting rules [15].

Fig. 9 Ratios of spectra as in Fig. 8 with predictions from the statistical quark model [6] which applies to the "direct" meson production at large x. The strange quark suppression factor is chosen as $\lambda = 0.3$.

Fig. 10 Single inclusive spectra as in Fig. 8 compared with the "quark stripping" model [7] which relates the jets initiated by hadrons as in our experiment to a superposition of quark jets by eq. 3.3. The Field Feynman model [24] is used for the quark fragmentation functions $D_V^{H'}(x)$ with $\lambda = 0.5$. The recently measured value $\lambda = 0.2$ [26] would bring the predictions for $K^{\pm}$ closer to our data. The excess in $\pi^- \to \pi^{\pm}$, $K^- \to K^-$ can be related to diffraction dissociation.

Fig. 11 Particle ratios and comparison to "quark stripping" model as specified in Fig. 10.

Fig. 12 Single pion production spectra from our experiment (full data points) and comparison to "quark stripping" model as in Fig. 10 (solid lines). We also show for comparison the corresponding combination of D_V^H functions derived from νp scattering [27] indicated by open data points. The dual parton model [8,9] where the fragmentation functions are folded with the quark distribution U_V (eq. 3.14) yields hadron spectra which tend to fall steeper than the data (dashed lines).

Fig. 13 Comparison of $\bar{u}$ quark distributions inside π^- and K^- beam particles as determined from lepton pair production [30] with corresponding π^o distributions from our experiment. The recombination model predicts these ratios to become equal at large x [10,12].

Fig. 14 QCD diagrams used in the derivation of counting rule predictions [15] which are displayed in Fig. 8.

Fig. 15 p_T dependence of invariant cross-sections for different intervals in $x = p_{ll}/p_{lab}$. The curves represent fits to the form (4.1). The errors include the systematic errors from particle identification but not the overall normalisation uncertainty of 8%.

Fig. 16 $p_T$dependence of invariant cross-sections as in Fig. 15.

Fig. 17 $p_T$dependence of invariant cross-sections as in Fig. 15.

Fig. 18 The parameters A, M from fits of eq. 4.1 to the spectra in Figs. 15-17, as well as $\langle p_T \rangle$ as function of x.

Fig. 19 Comparison of some representative p_T spectra from our experiment with the results from refs. [16,17].

Fig. 20 p_T dependence of ratios of invariant cross-sections for $0.6 < x < 0.8$ for different particle types. Final particles with the same mass show a similar p_T dependence, whereas the K/π ratios increase.

Fig. 21 Particle ratio π^+/π^- and h^+/h^- of unidentified charged hadrons (taken as pions) for fixed $x_R = 2 E_{CM}/\sqrt{s}$ vs. CMS scattering angle Θ_{CM}. The absence of a sizable variation for $\Theta_{CM} < 60°$ and smooth connection to the large p_T measurements at 200 GeV/c [32] suggest the same dynamic origin of leading and non-leading mesons. Also shown is the prediction of a hard scattering QCD model [35] which is consistent with both sets of data.

Fig. 22 Distribution of charged hadrons h_2^+ and h_2^- in the remaining energy x' after removing the negative hadron h_1^- with energy x_1.

Fig. 23 Ratios of spectra of charged hadrons h_2^+ and h_2^- as in Fig. 22 for different intervals in x_1 of the negative trigger hadron h_1^- in comparison with simple models (see text) with a "held back" quark and "flying through" quark. The data require that both valence quarks contribute to the forward fragmentation with $x \geq 0.2$.

Fig. 24 Comparison of charged particle correlations as in Fig. 22 with the model of Fukuda et al. [42] which incorporates fragmentation and recombination mechanisms.

Fig.25 Correlation ratios as in Fig. 23 but with a cut in the two particle invariant mass to remove low mass diffraction. The discrepancy to the "held back" quark remains.

Fig. 26 Ratios of spectra of charged hadrons h_2^+ and h_2^- as in Fig. 23, but with $x_2 \geq 0.5$ and as function of the p_T of the negative trigger particle h_1^-. At small x_1 this ratio becomes negative (with increasing p_T) reflecting the negatively charged spectator quark; at higher x_1 the ratio is still far away from the value 3.5 expected for a single quark jet.

TABLE I: Threshold momenta p_{th}^{h} [GeV/c] for the two Cerenkov counters.

	π	K	p
C1	8.1	28.4	54.0
C2	18.1	64.0	100.0

TABLE IIa: p_T integrated invariant cross-sections $\sigma_{in}\, \rho(x) \approx x/\pi\, d\sigma/dx$ (eq. 3.1) in mb. Errors include systematic errors but not the overall normalisation uncertainty of 8%.

x	$\pi^- \to \pi^-$	$\pi^- \to \pi^+$	$K^- \to \pi^-$	$K^- \to \pi^+$
0.20-0.25	3.33 ± 0.16	1.97 ± 0.09	2.12 ± 0.13	1.58 ± 0.08
0.25-0.30	2.98 ± 0.14	1.65 ± 0.08	1.74 ± 0.11	1.25 ± 0.06
0.30-0.35	2.62 ± 0.13	1.33 ± 0.07	1.54 ± 0.09	1.02 ± 0.05
0.35-0.40	2.42 ± 0.12	1.02 ± 0.05	1.24 ± 0.08	0.74 ± 0.04
0.40-0.45	2.10 ± 0.10	0.89 ± 0.05	1.11 ± 0.07	0.59 ± 0.04
0.45-0.50	1.89 ± 0.09	0.70 ± 0.04	0.89 ± 0.06	0.47 ± 0.03
0.50-0.55	1.65 ± 0.09	0.53 ± 0.04	0.77 ± 0.05	0.35 ± 0.03
0.55-0.60	1.63 ± 0.09	0.44 ± 0.03	0.58 ± 0.04	0.28 ± 0.02
0.60-0.65	1.53 ± 0.08	0.36 ± 0.03	0.45 ± 0.04	0.21 ± 0.02
0.65-0.70	1.61 ± 0.08	0.32 ± 0.03	0.39 ± 0.04	0.13 ± 0.02
0.70-0.75	1.57 ± 0.08	0.27 ± 0.02	0.24 ± 0.04	0.093 ± 0.013
0.75-0.80	1.68 ± 0.09	0.26 ± 0.02	0.19 ± 0.04	0.053 ± 0.010
0.80-0.85	1.68 ± 0.14	0.23 ± 0.02	0.20 ± 0.04	0.056 ± 0.011
0.85-0.90	1.91 ± 0.16	0.21 ± 0.02	0.14 ± 0.04	0.014 ± 0.005
0.90-0.95	2.64 ± 0.22	0.11 ± 0.015		0.004 ± 0.003
0.95-1.00		0.020 ± 0.006		

TABLE IIb: Same as Table IIa but for kaons.

x	$\pi^- \to K^-$	$\pi^- \to K^+$	$K^- \to K^-$	$K^- \to K^+$
0.50-0.55			1.02 ± 0.08	
0.55-0.60			1.01 ± 0.07	
0.60-0.65	0.13 ± 0.02	0.076 ± 0.014	0.98 ± 0.06	0.027 ± 0.009
0.65-0.70	0.15 ± 0.02	0.048 ± 0.012	0.90 ± 0.06	0.024 ± 0.008
0.70-0.75	0.10 ± 0.02	0.046 ± 0.009	0.93 ± 0.06	0.007 ± 0.004
0.75-0.80	0.090 ± 0.014	0.025 ± 0.007	0.96 ± 0.06	0.008 ± 0.004
0.80-0.85	0.075 ± 0.015	0.027 ± 0.007	1.03 ± 0.07	0.006 ± 0.004
0.85-0.90	0.075 ± 0.014	0.008 ± 0.004	1.14 ± 0.08	0.002 ± 0.001
0.90-0.95		0.008 ± 0.004	1.79 ± 0.14	
0.95-1.00				

TABLE IIc: Same as Table IIa but for π°'s. The first column refers to the measured range $p_T < 0.8$ GeV/c, the second to the full range using the fit to eq. 4.1

x	$\pi^- \to \pi^\circ$		$K^- \to \pi^\circ$	
	$p_T < 0.8$ GeV/c	all p_T	$p_T < 0.8$ GeV/c	all p_T
0.4 - 0.5	1.04 ± 0.05	1.32 ± 0.08	0.63 ± 0.04	0.78 ± 0.07
0.5 - 0.6	0.76 ± 0.03	0.92 ± 0.05	0.46 ± 0.03	0.54 ± 0.04
0.6 - 0.7	0.60 ± 0.03	0.70 ± 0.04	0.32 ± 0.02	0.37 ± 0.03
0.7 - 0.8	0.50 ± 0.03	0.50 ± 0.03	0.22 ± 0.02	0.22 ± 0.03
0.8 - 0.9	0.36 ± 0.02	0.38 ± 0.02	0.11 ± 0.01	0.11 ± 0.02
0.9 - 1.0	0.25 ± 0.02	0.26 ± 0.02	0.04 ± 0.01	0.06 ± 0.02

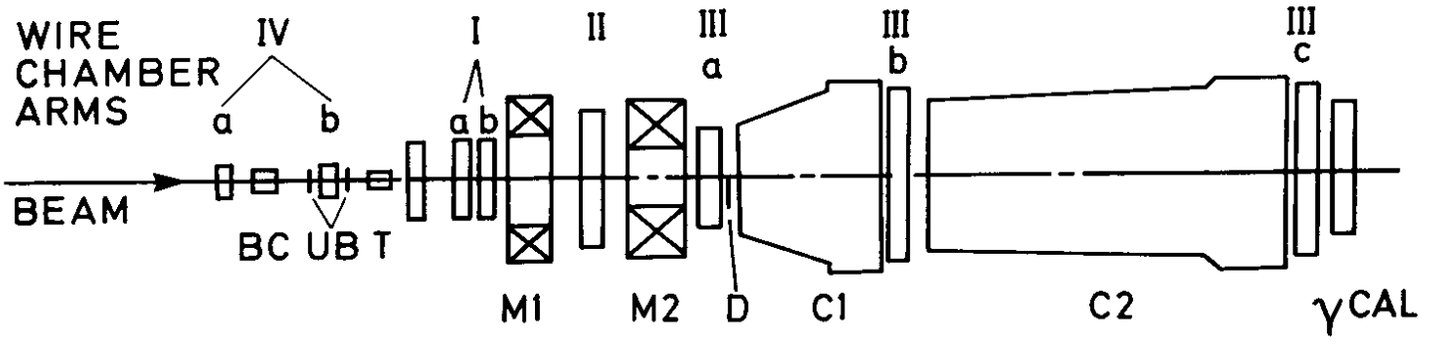
WIRE
CHAMBER
ARMS
IV
a
b
I
a b
II
III
a
III
b
III
c
BEAM
BC UB T
M1
M2
D
C1
C2
γCAL

Fig. 1

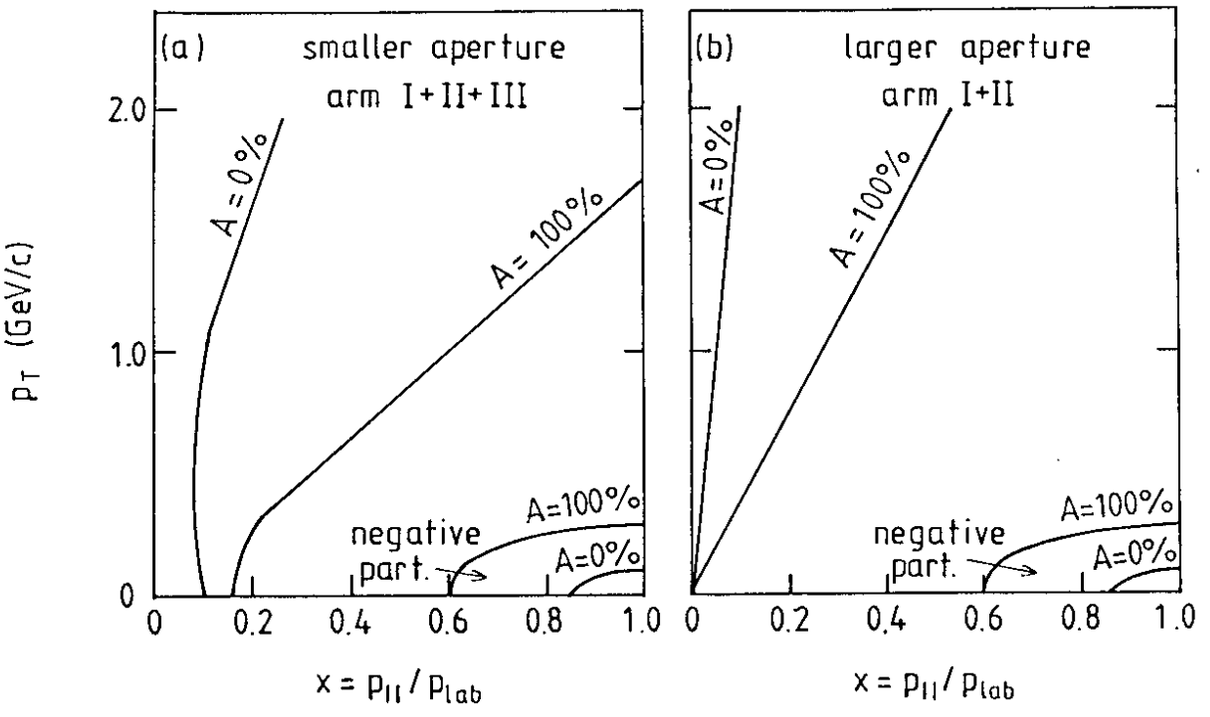
(a)
smaller aperture
arm I+II+III
(b)
larger aperture
arm I+II
A=0%
A=100%
negative
part.
A=100%
A=0%
p_T (GeV/c)
2.0
1.0
0
0.2
0.4
0.6
0.8
1.0
$x = p_{II} / p_{lab}$

Fig. 2

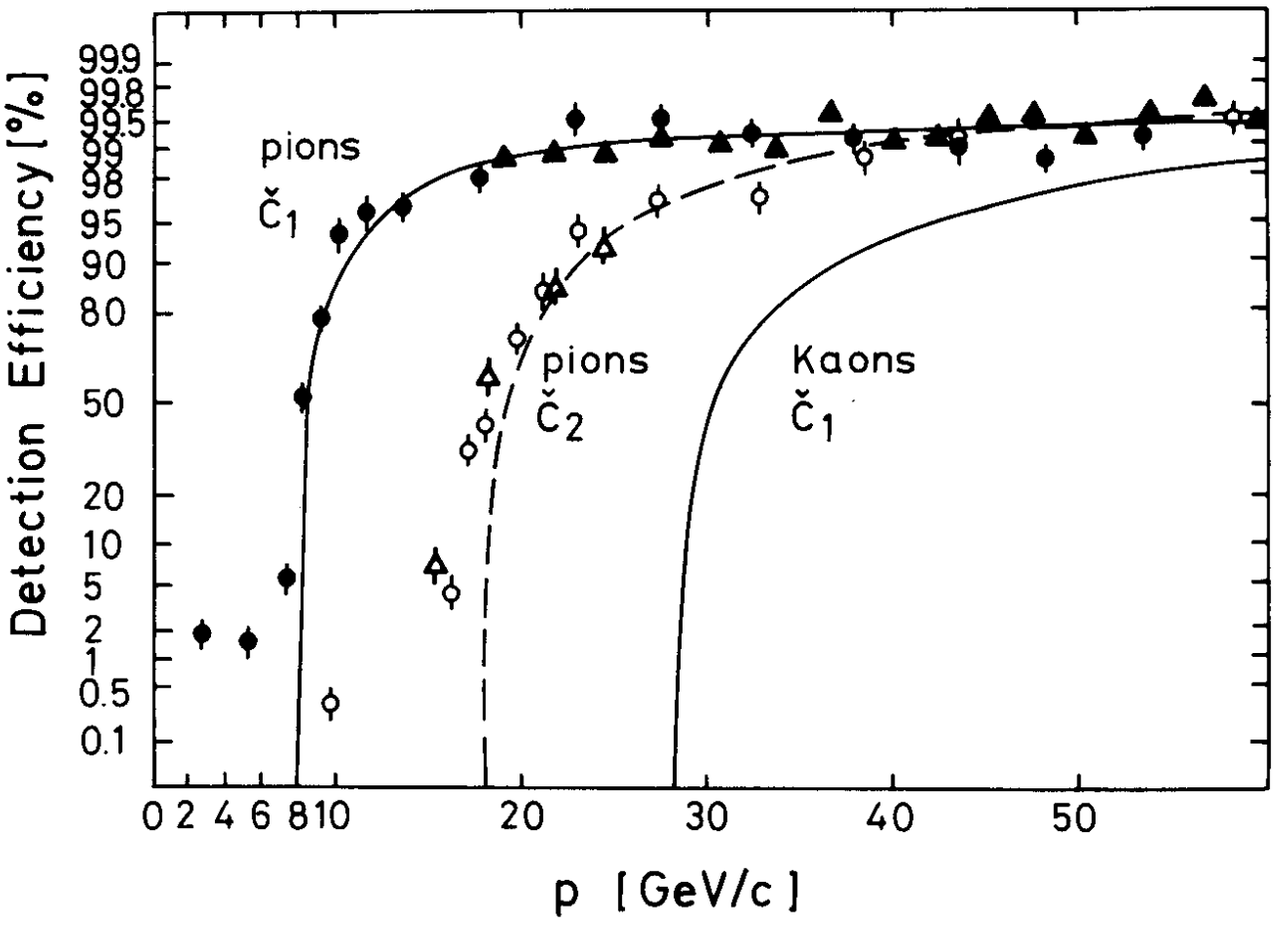
Detection Efficiency [%]
99.9
99.8
99.5
98
95
90
80
50
20
10
5
2
1
0.5
0.1
pions
$\check{C}_1$
pions
$\check{C}_2$
Kaons
$\check{C}_1$
0 2 4 6 8 10
20
30
40
50
p [GeV/c]

Fig. 3

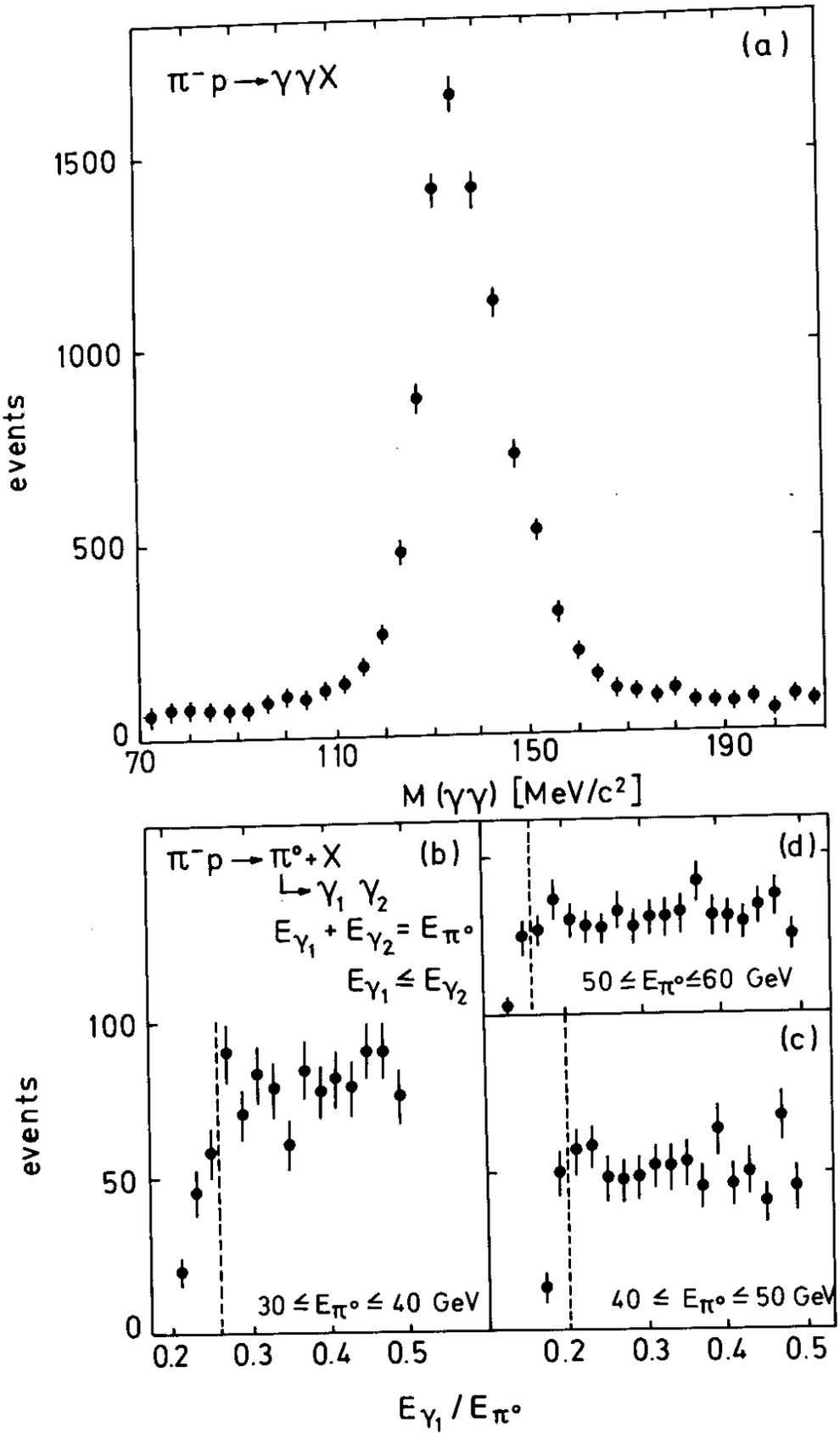
(a)
$\pi^- p \rightarrow \gamma\gamma X$
1500
1000
500
0
events
70
110
150
190
M ($\gamma\gamma$) [MeV/c^2]
$\pi^- p \rightarrow \pi^0 + X$
(b)
$\hookrightarrow \gamma_1\ \gamma_2$
$E_{\gamma_1} + E_{\gamma_2} = E_{\pi^0}$
$E_{\gamma_1} \leq E_{\gamma_2}$
(d)
$50 \leq E_{\pi^0} \leq 60$ GeV
(c)
100
50
0
events
$30 \leq E_{\pi^0} \leq 40$ GeV
$40 \leq E_{\pi^0} \leq 50$ GeV
0.2
0.3
0.4
0.5
E_{γ_1} / E_{π^0}

Fig. 4

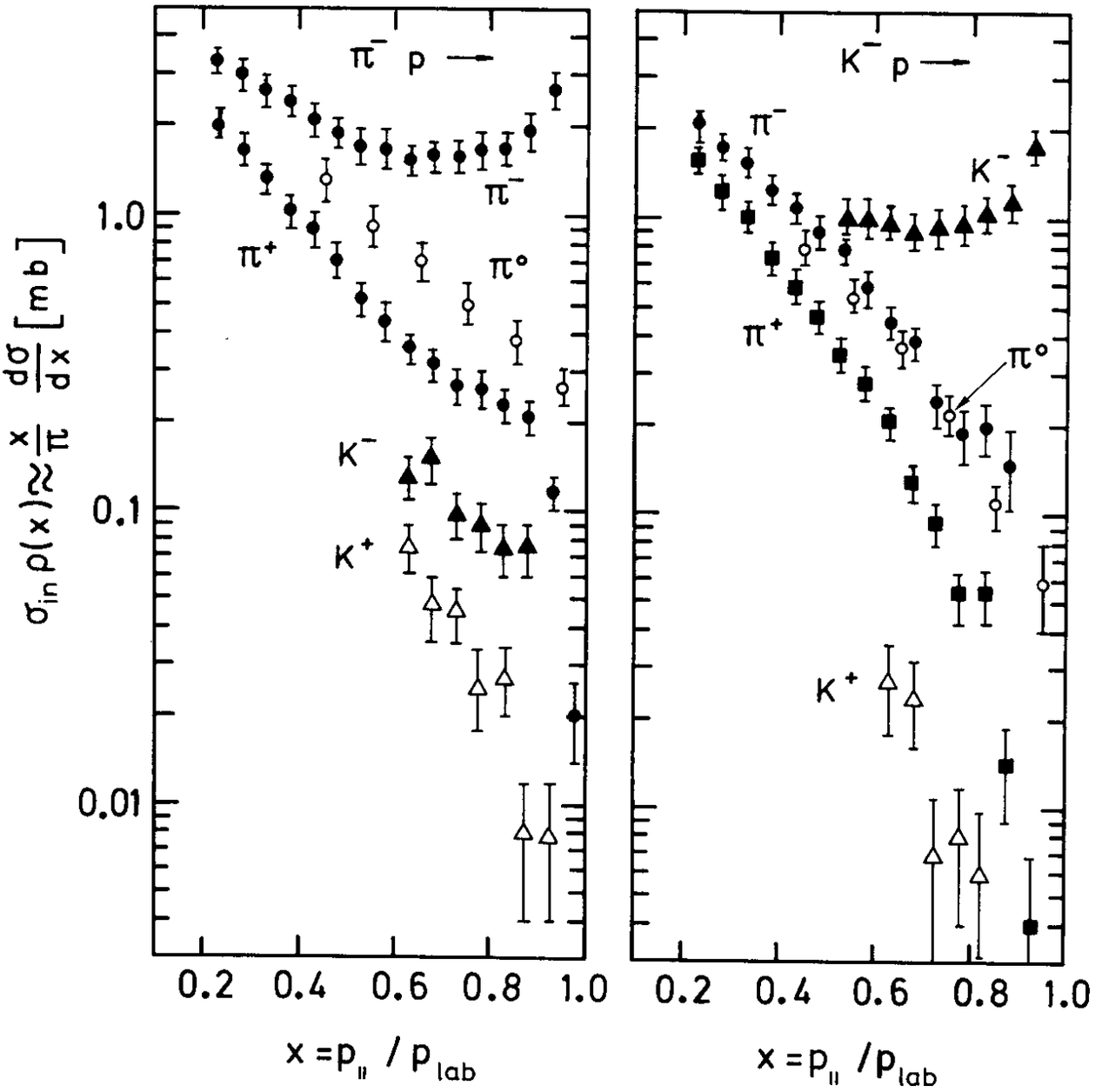
$\pi^- p \rightarrow$
π^-
π^+
π°
K^-
K^+
$K^- p \rightarrow$
π^-
K^-
π^+
π°
K^+
$\sigma_{in}\,\rho(x) \approx \frac{x}{\pi}\,\frac{d\sigma}{dx}$ [mb]
1.0
0.1
0.01
0.2
0.4
0.6
0.8
1.0
$x = p_{\parallel} / p_{lab}$

Fig. 5

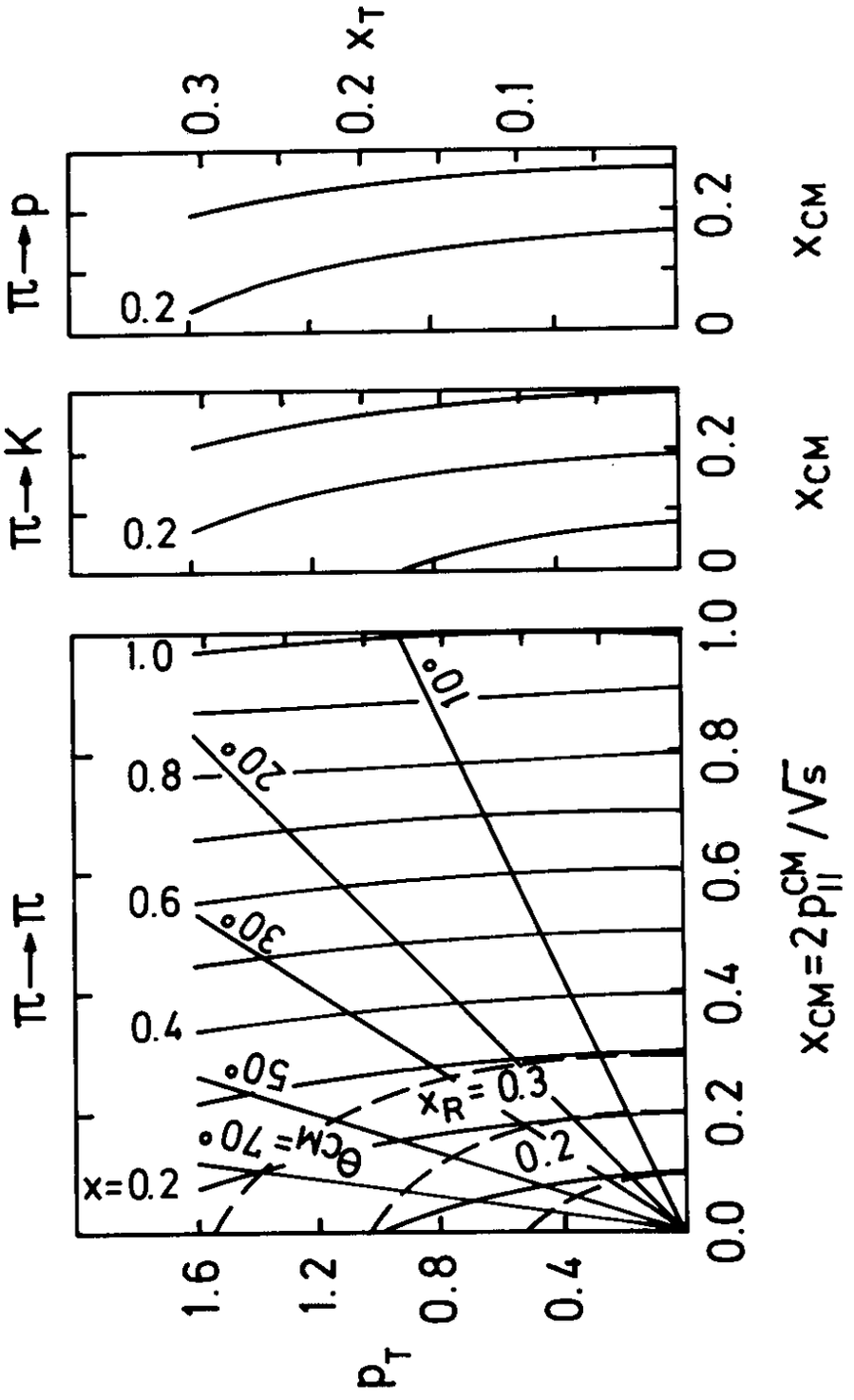
π→p
0.2
0.3
0.2 xT
0.1
0
0.2
xCM
π→K
0.2
0
0.2
xCM
π→π
1.0
0.8
0.6
0.4
x=0.2
10°
20°
30°
50°
θCM=70°
xR=0.3
0.2
0.0
0.2
0.4
0.6
0.8
1.0
xCM=2pCM∥/√s
1.6
1.2
0.8
0.4
pT

Fig. 6

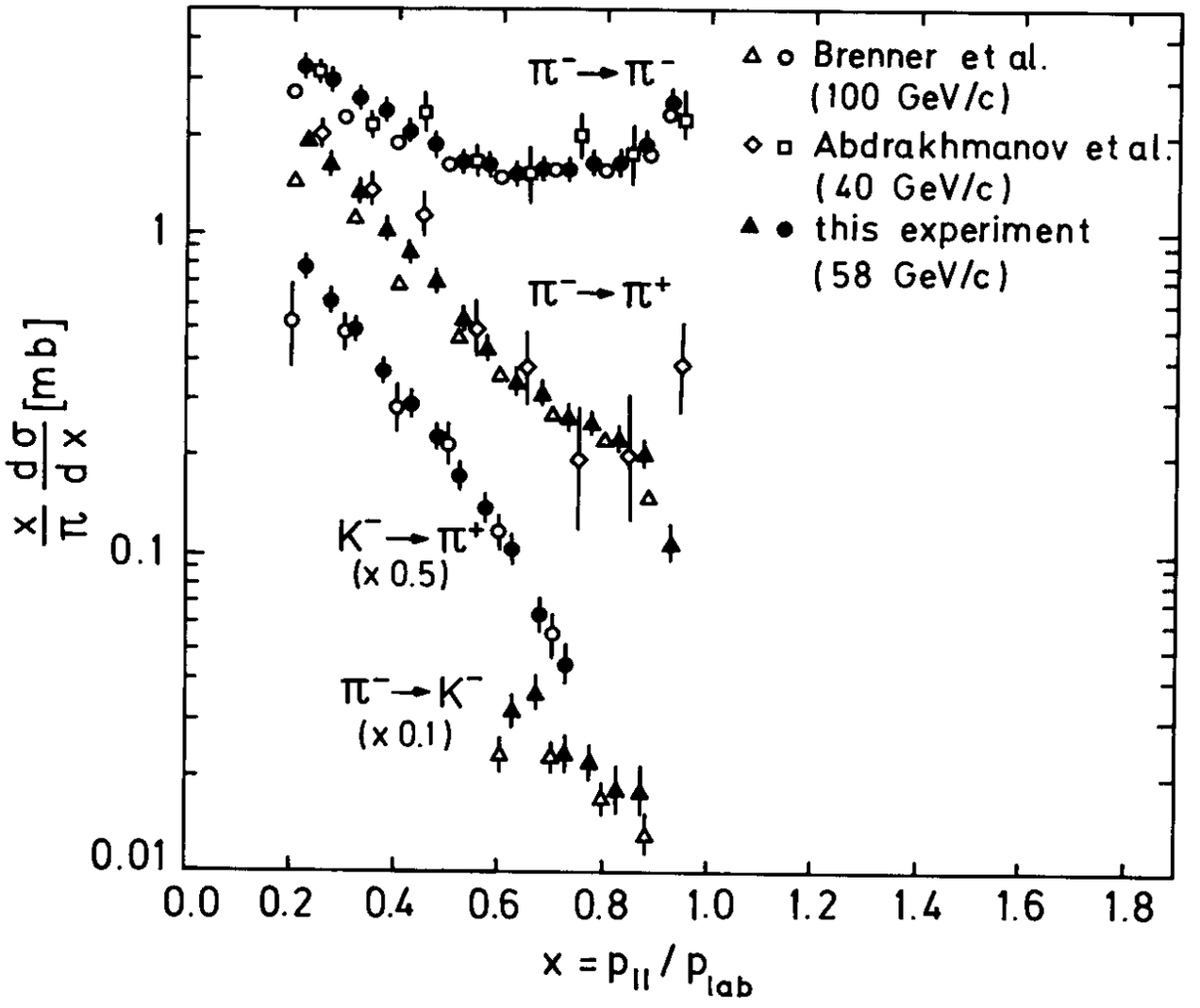
Brenner et al.
(100 GeV/c)
Abdrakhmanov et al.
(40 GeV/c)
this experiment
(58 GeV/c)
π⁻→π⁻
π⁻→π⁺
K⁻→π⁺
(x 0.5)
π⁻→K⁻
(x 0.1)
x d σ/π d x [mb]
1
0.1
0.01
0.0
0.2
0.4
0.6
0.8
1.0
1.2
1.4
1.6
1.8
x = p_II / p_lab

Fig. 7

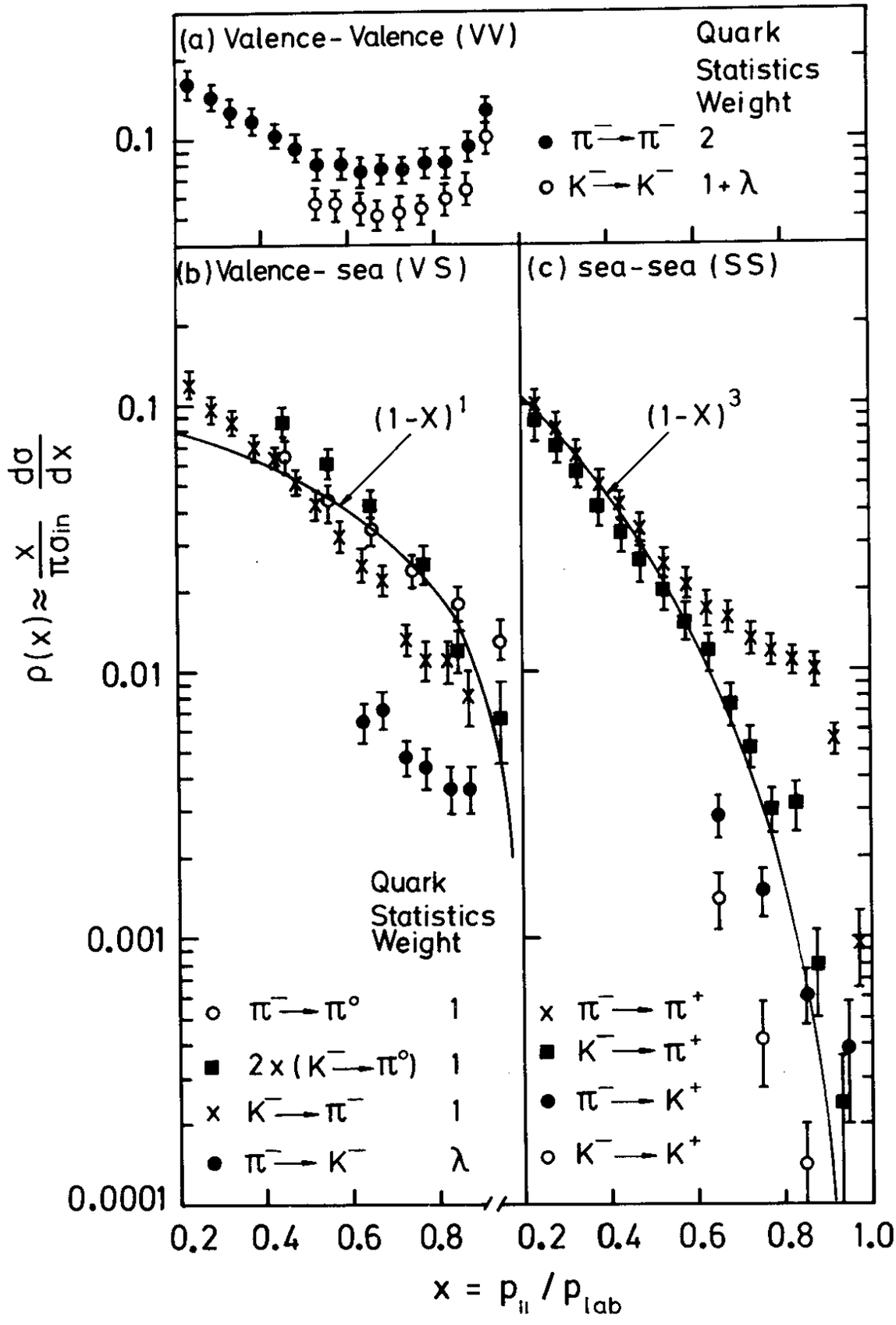
(a) Valence - Valence (VV)
Quark Statistics Weight
π⁻ → π⁻ 2
K⁻ → K⁻ 1+λ
(b) Valence - sea (VS)
(c) sea - sea (SS)
(1-X)¹
(1-X)³
Quark Statistics Weight
π⁻ → π° 1
2 x (K⁻ → π°) 1
K⁻ → π⁻ 1
π⁻ → K⁻ λ
π⁻ → π⁺
K⁻ → π⁺
π⁻ → K⁺
K⁻ → K⁺
ρ(x) ≈ x/(πσin) dσ/dx
0.1
0.01
0.001
0.0001
0.2 0.4 0.6 0.8
0.2 0.4 0.6 0.8 1.0
x = p|| / plab

Fig. 8

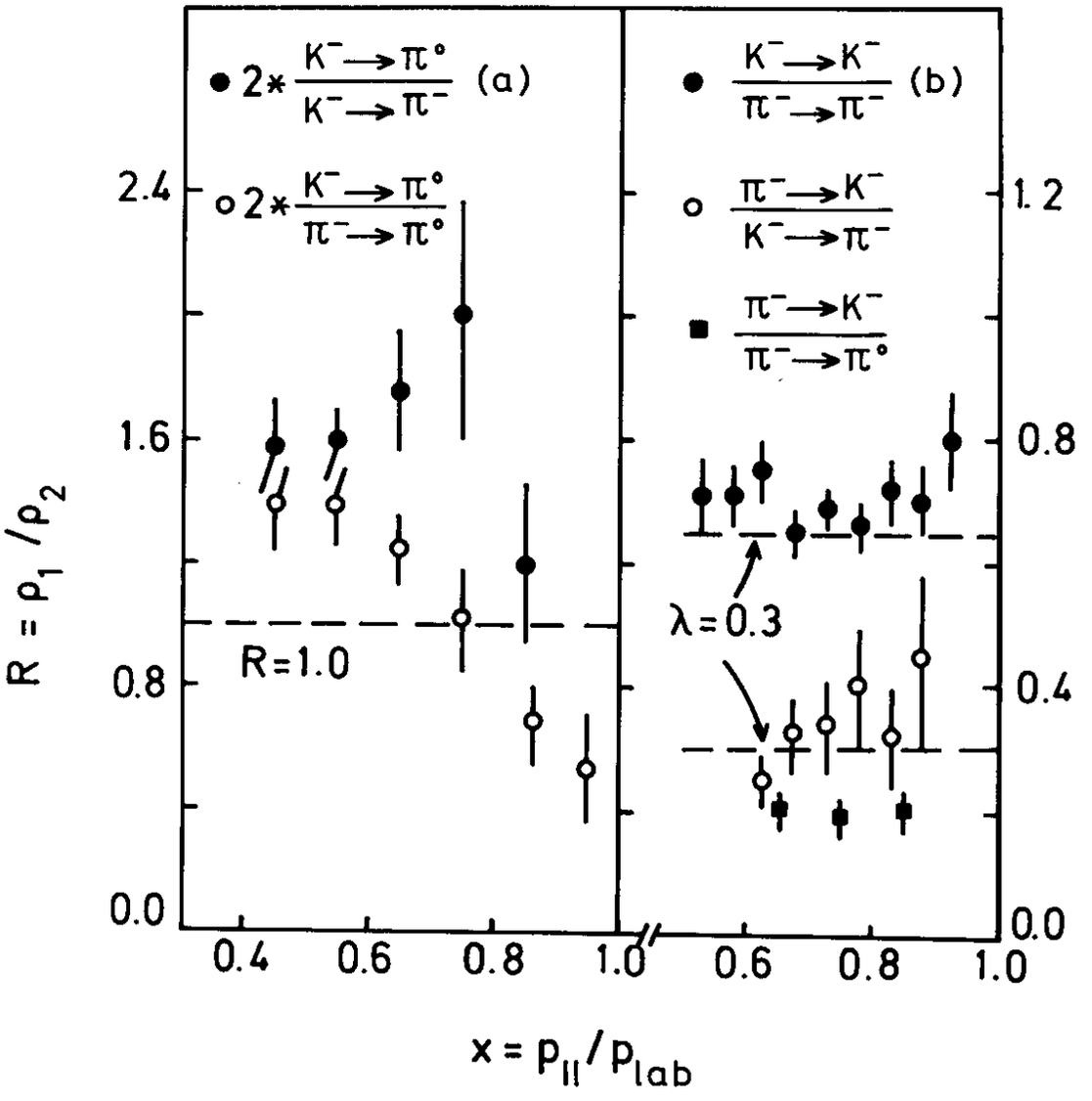
● 2* K⁻→π° / K⁻→π⁻ (a)
○ 2* K⁻→π° / π⁻→π°
● K⁻→K⁻ / π⁻→π⁻ (b)
○ π⁻→K⁻ / K⁻→π⁻
■ π⁻→K⁻ / π⁻→π°
R=1.0
λ=0.3
R = ρ1 / ρ2
x = p|| / plab
2.4
1.6
0.8
0.0
1.2
0.8
0.4
0.0
0.4
0.6
0.8
1.0
0.6
0.8
1.0

Fig. 9

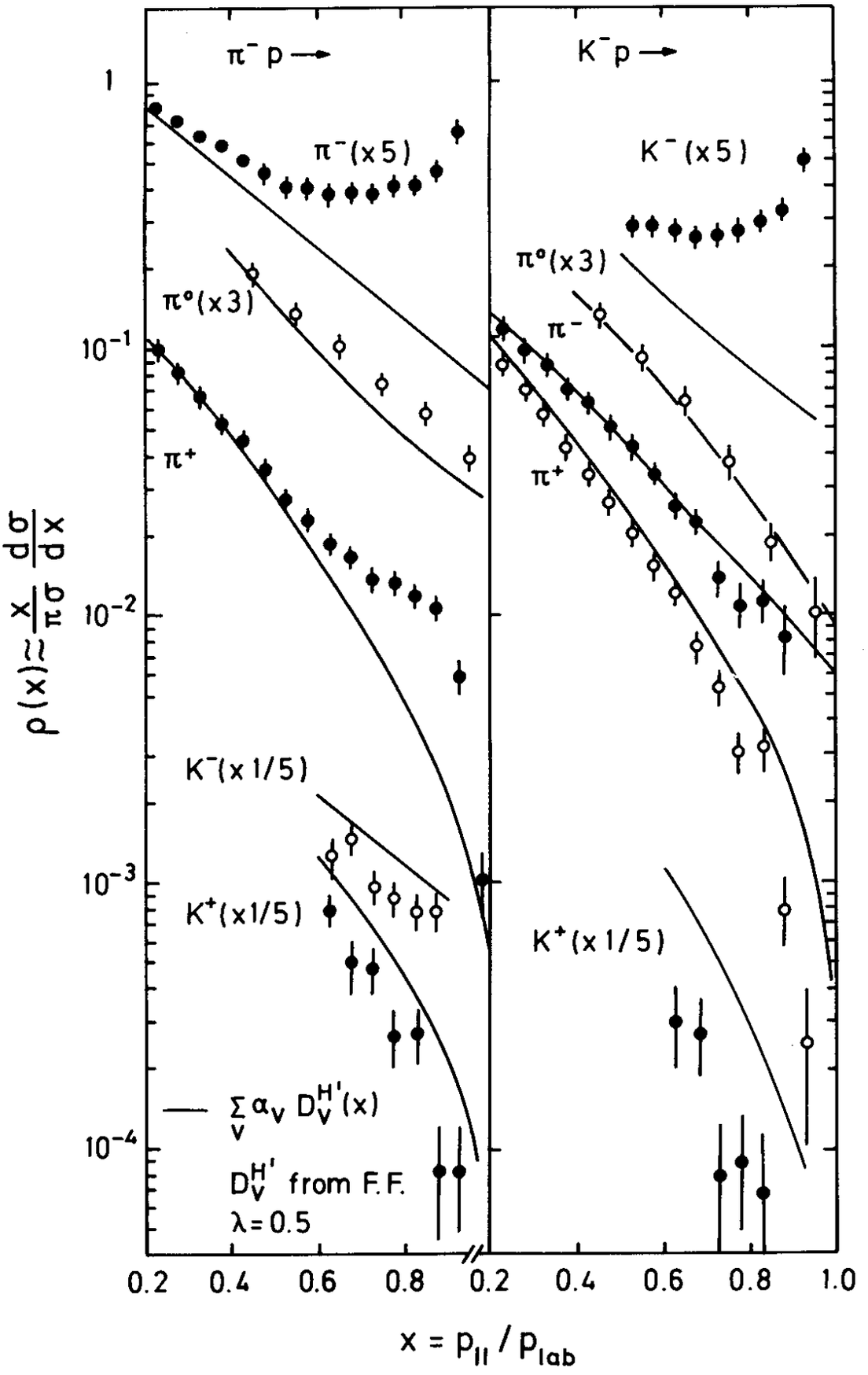
π⁻ p →
K⁻ p →
π⁻(x5)
K⁻(x5)
π°(x3)
π°(x3)
π⁻
π⁺
π⁺
K⁻(x1/5)
K⁺(x1/5)
K⁺(x1/5)
Σ α_V D_V^H'(x)
D_V^H' from F.F.
λ=0.5
ρ(x) ≃ x/πσ dσ/dx
x = p_II / p_lab
1
10⁻¹
10⁻²
10⁻³
10⁻⁴
0.2
0.4
0.6
0.8
1.0

Fig. 10

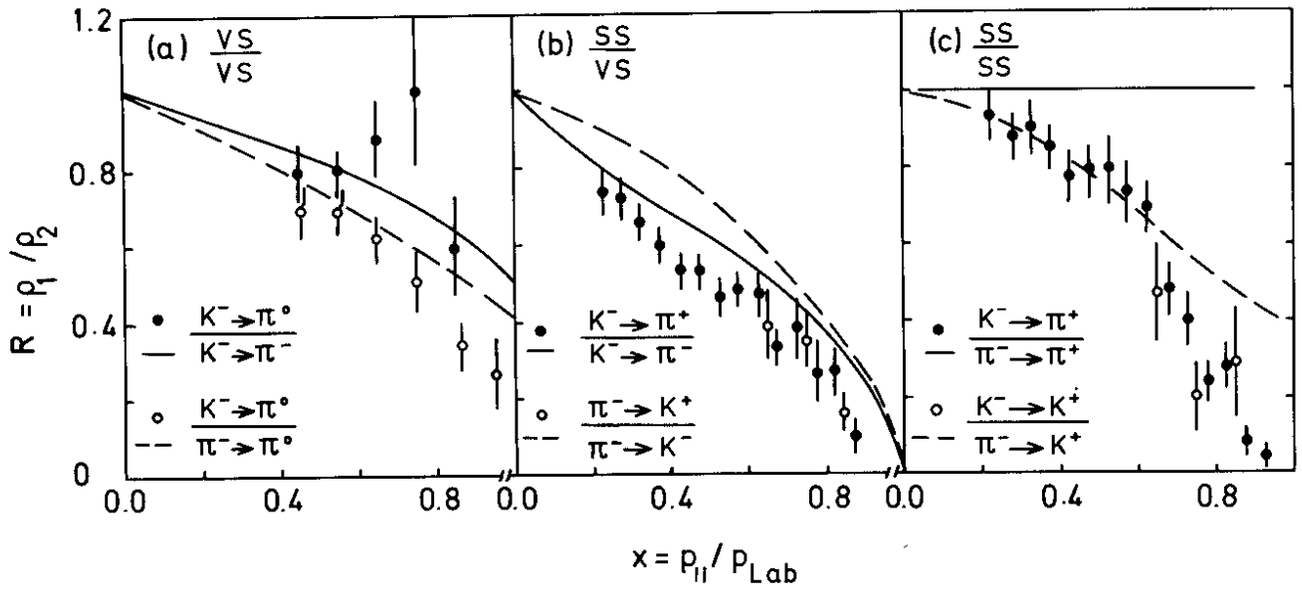

Fig. 11

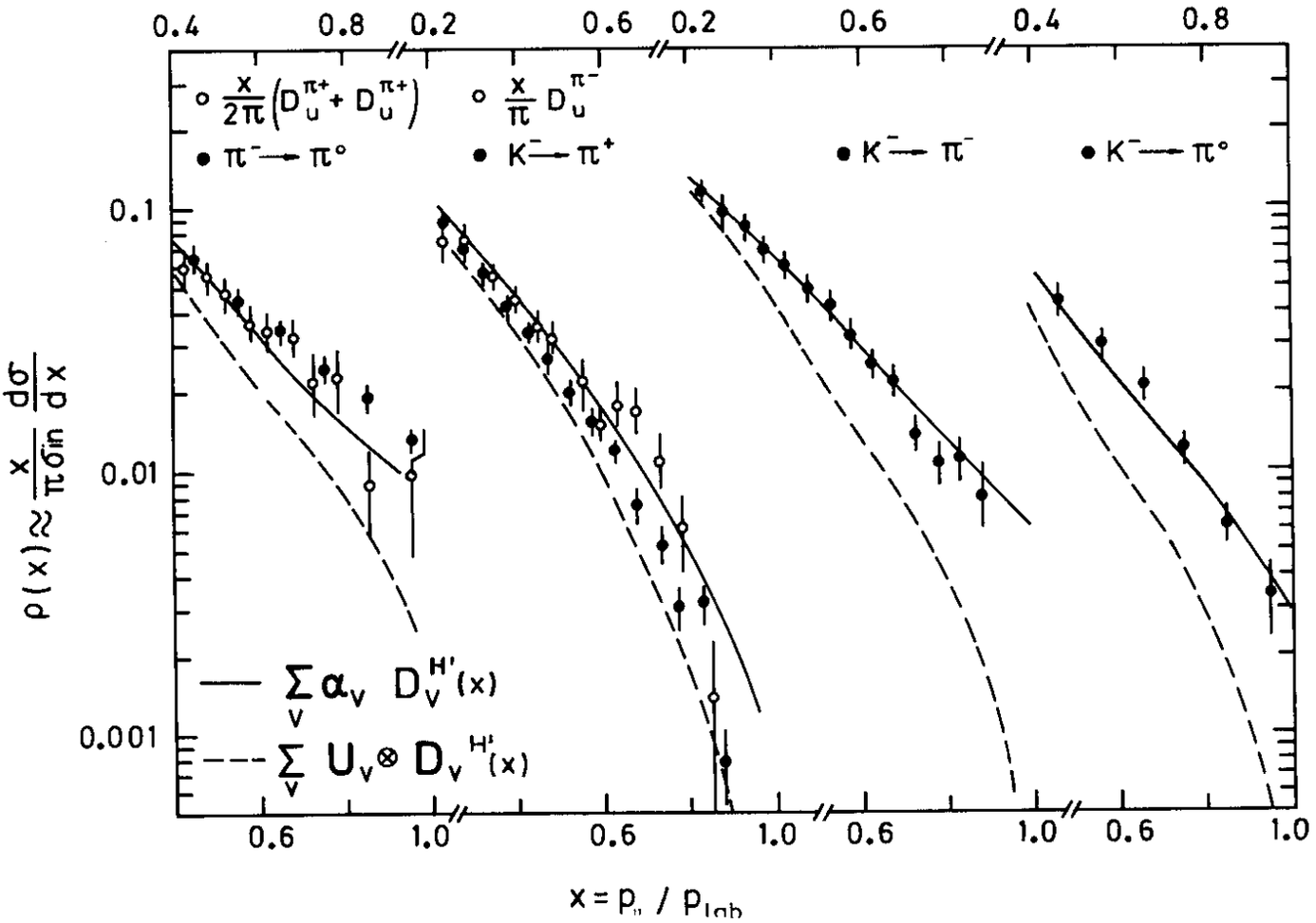

Fig. 12

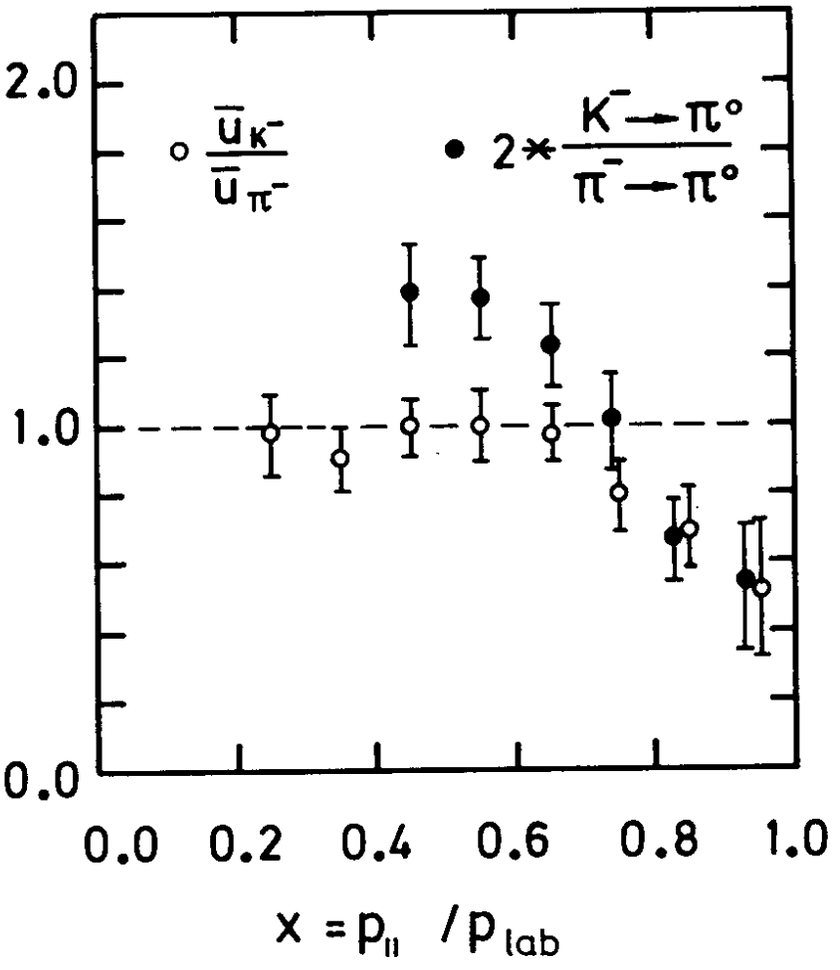
2.0
1.0
0.0
0.0 0.2 0.4 0.6 0.8 1.0
$\circ \frac{\bar{u}_{K^-}}{\bar{u}_{\pi^-}}$
$\bullet\ 2* \frac{K^- \to \pi^\circ}{\pi^- \to \pi^\circ}$
$x = p_{\parallel} / p_{lab}$

Fig. 13

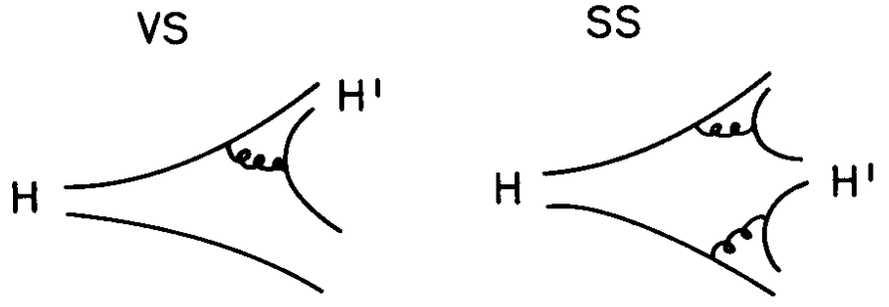
VS
H
H'
SS
H
H'

Fig. 14

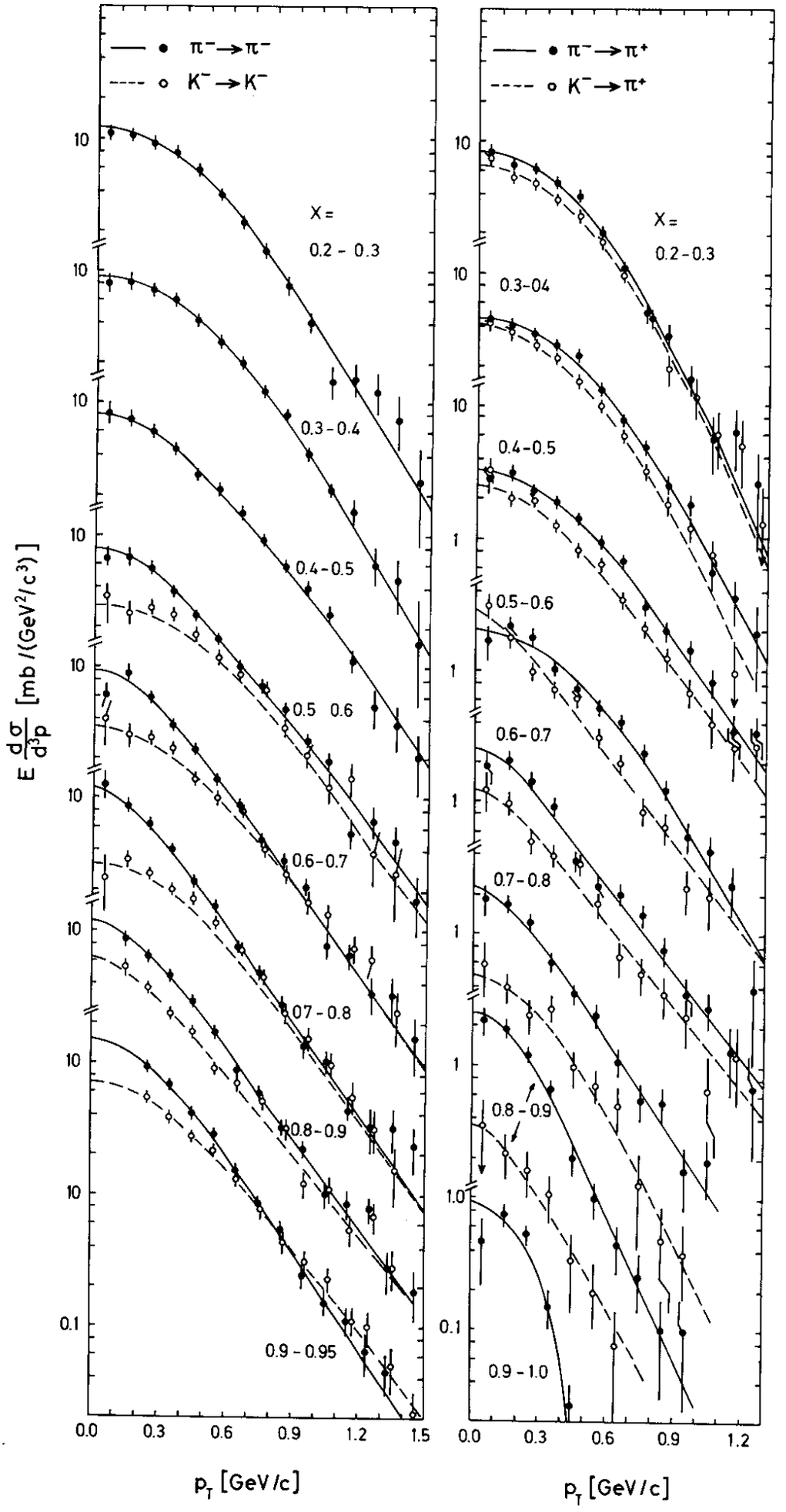
π⁻→π⁻
K⁻→K⁻
π⁻→π⁺
K⁻→π⁺
X =
0.2 - 0.3
0.3-04
0.3-0.4
0.4-0.5
0.5 0.6
0.5-0.6
0.6-0.7
0.7-0.8
0.07 - 0.8
0.8-0.9
0.9 - 0.95
0.9 - 1.0
E dσ/d³p [mb/(GeV²/c³)]
p_T [GeV/c]
p_T [GeV/c]

Fig. 15

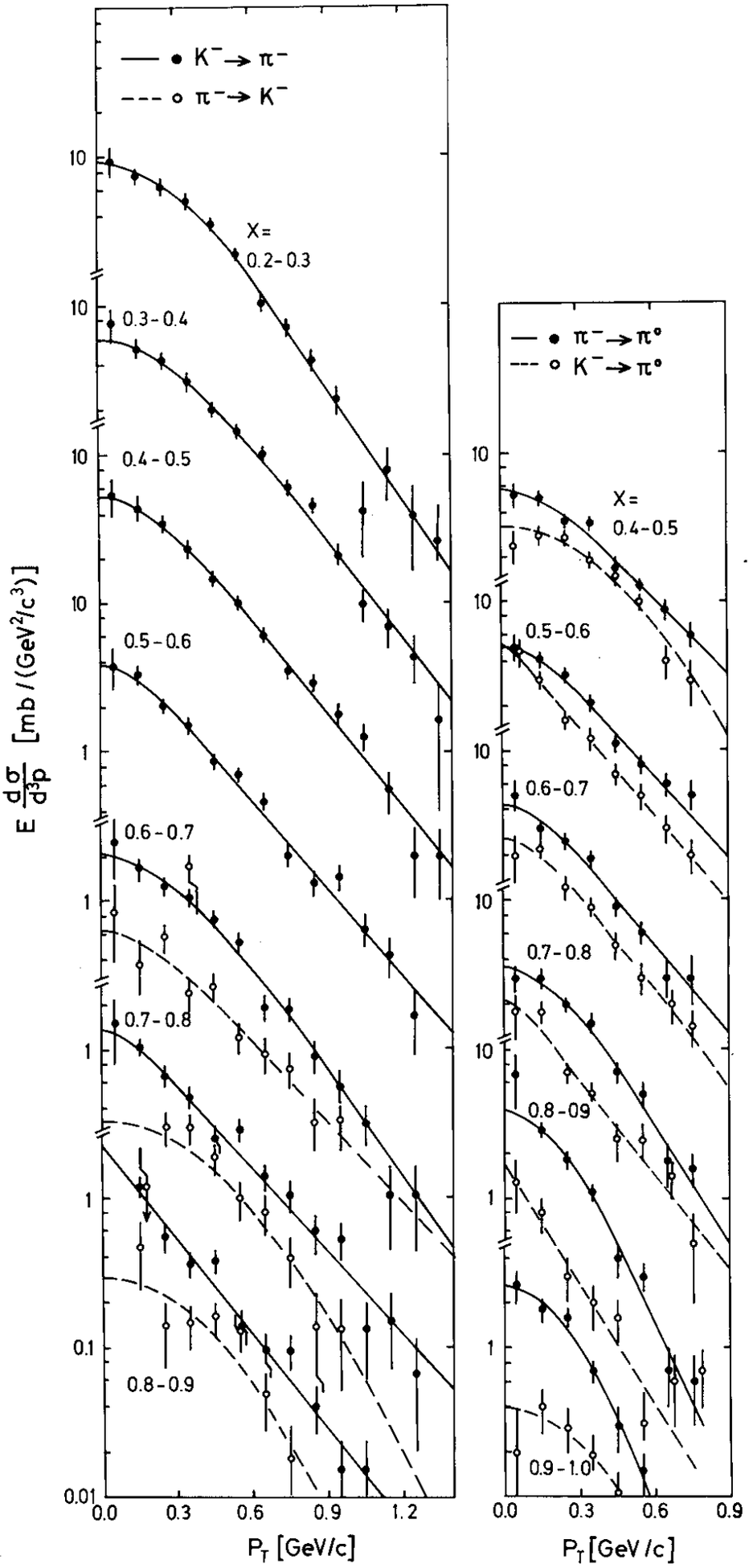
K⁻→ π⁻
π⁻→ K⁻
X=
0.2-0.3
0.3-0.4
0.4-0.5
0.5-0.6
0.6-0.7
0.7-0.8
0.8-0.9
E dσ/d³p [mb/(GeV²/c³)]
P_T [GeV/c]
π⁻→ π°
K⁻→ π°
X=
0.4-0.5
0.5-0.6
0.6-0.7
0.7-0.8
0.8-09
0.9-1.0
P_T [GeV/c]

Fig. 16

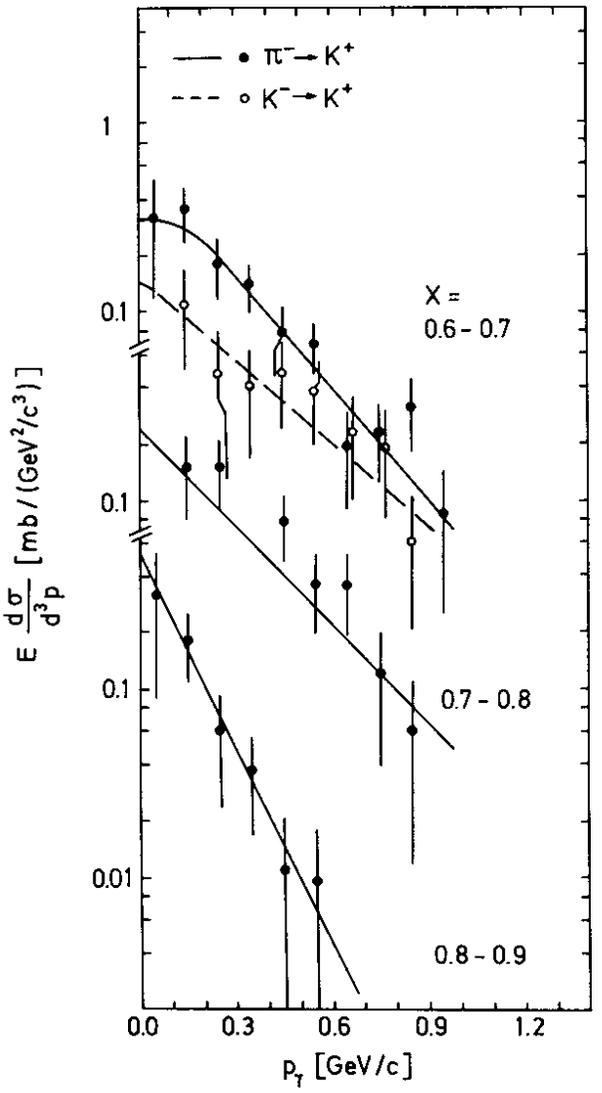
π⁻→K⁺
K⁻→K⁺
X =
0.6 - 0.7
0.7 - 0.8
0.8 - 0.9
1
0.1
0.1
0.1
0.01
0.0
0.3
0.6
0.9
1.2
p_T [GeV/c]
E dσ/d³p [mb/(GeV²/c³)]

Fig. 17

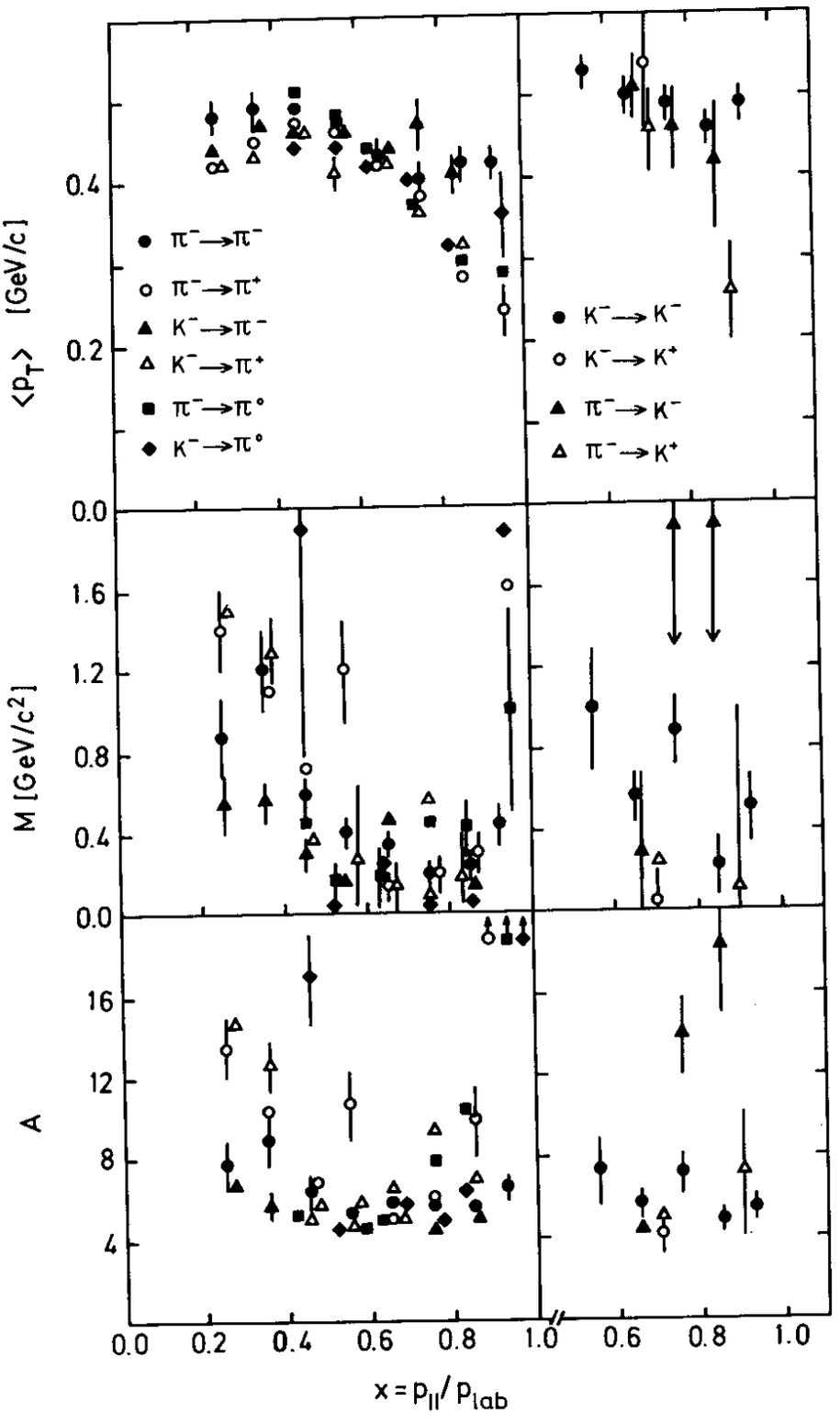
$\pi^- \to \pi^-$
$\pi^- \to \pi^+$
$K^- \to \pi^-$
$K^- \to \pi^+$
$\pi^- \to \pi^\circ$
$K^- \to \pi^\circ$
$K^- \to K^-$
$K^- \to K^+$
$\pi^- \to K^-$
$\pi^- \to K^+$
$\langle p_T \rangle$ [GeV/c]
M [GeV/c^2]
A
$x = p_{||} / p_{lab}$

Fig. 18

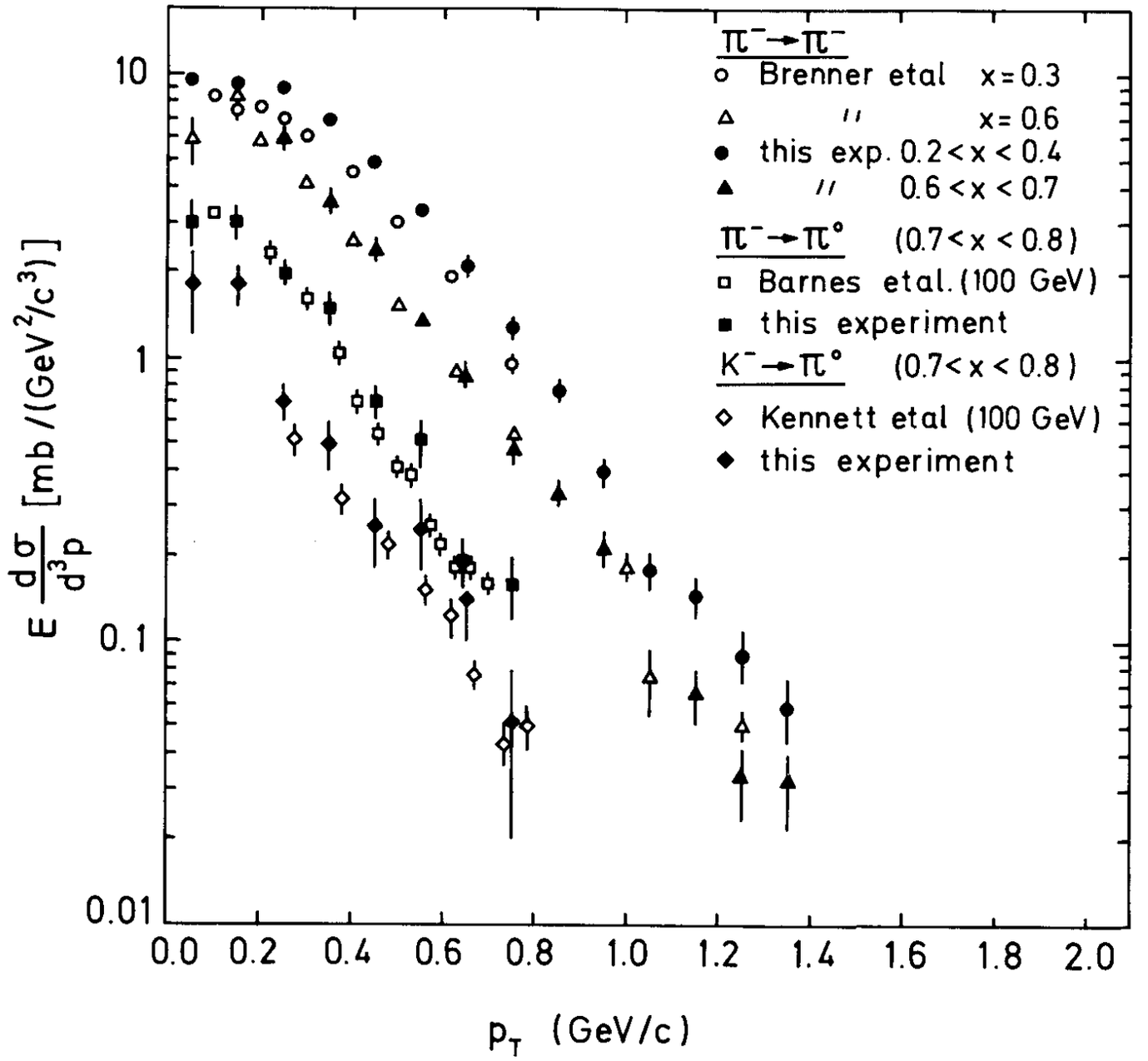
$\pi^- \to \pi^-$
Brenner etal x = 0.3
" x = 0.6
this exp. 0.2 < x < 0.4
" 0.6 < x < 0.7
$\pi^- \to \pi^\circ$ (0.7 < x < 0.8)
Barnes etal. (100 GeV)
this experiment
$K^- \to \pi^\circ$ (0.7 < x < 0.8)
Kennett etal (100 GeV)
this experiment
$E \frac{d\sigma}{d^3p}$ [mb/(GeV^2/c^3)]
p_T (GeV/c)
10
1
0.1
0.01
0.0
0.2
0.4
0.6
0.8
1.0
1.2
1.4
1.6
1.8
2.0

Fig. 19

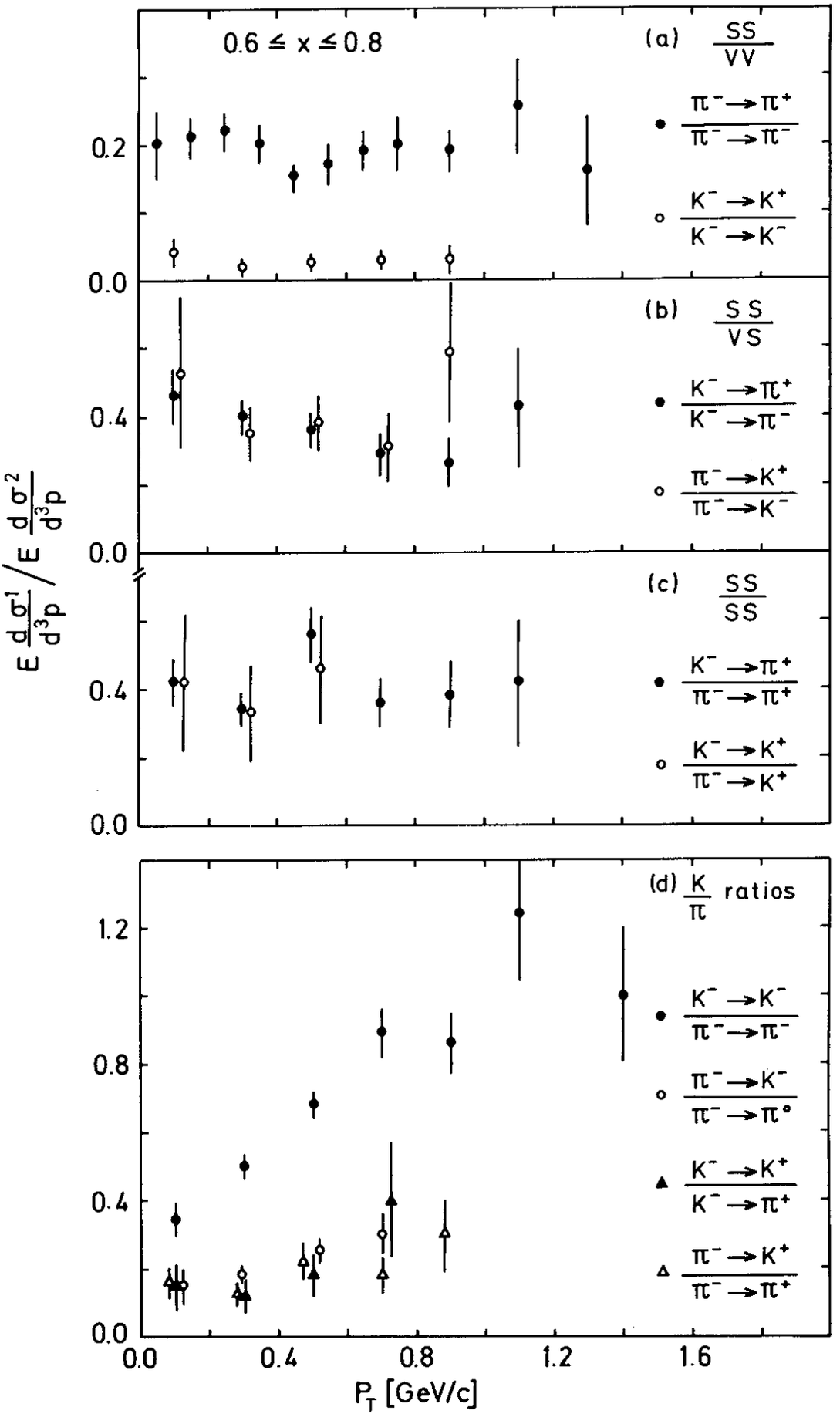
0.6 ≤ x ≤ 0.8
(a) SS/VV
π⁻→π⁺ / π⁻→π⁻
K⁻→K⁺ / K⁻→K⁻
(b) SS/VS
K⁻→π⁺ / K⁻→π⁻
π⁻→K⁺ / π⁻→K⁻
(c) SS/SS
K⁻→π⁺ / π⁻→π⁺
K⁻→K⁺ / π⁻→K⁺
(d) K/π ratios
K⁻→K⁻ / π⁻→π⁻
π⁻→K⁻ / π⁻→π°
K⁻→K⁺ / K⁻→π⁺
π⁻→K⁺ / π⁻→π⁺
E d σ¹/d³p / E d σ²/d³p
P_T [GeV/c]
0.0
0.4
0.8
1.2
1.6
0.2

Fig. 20

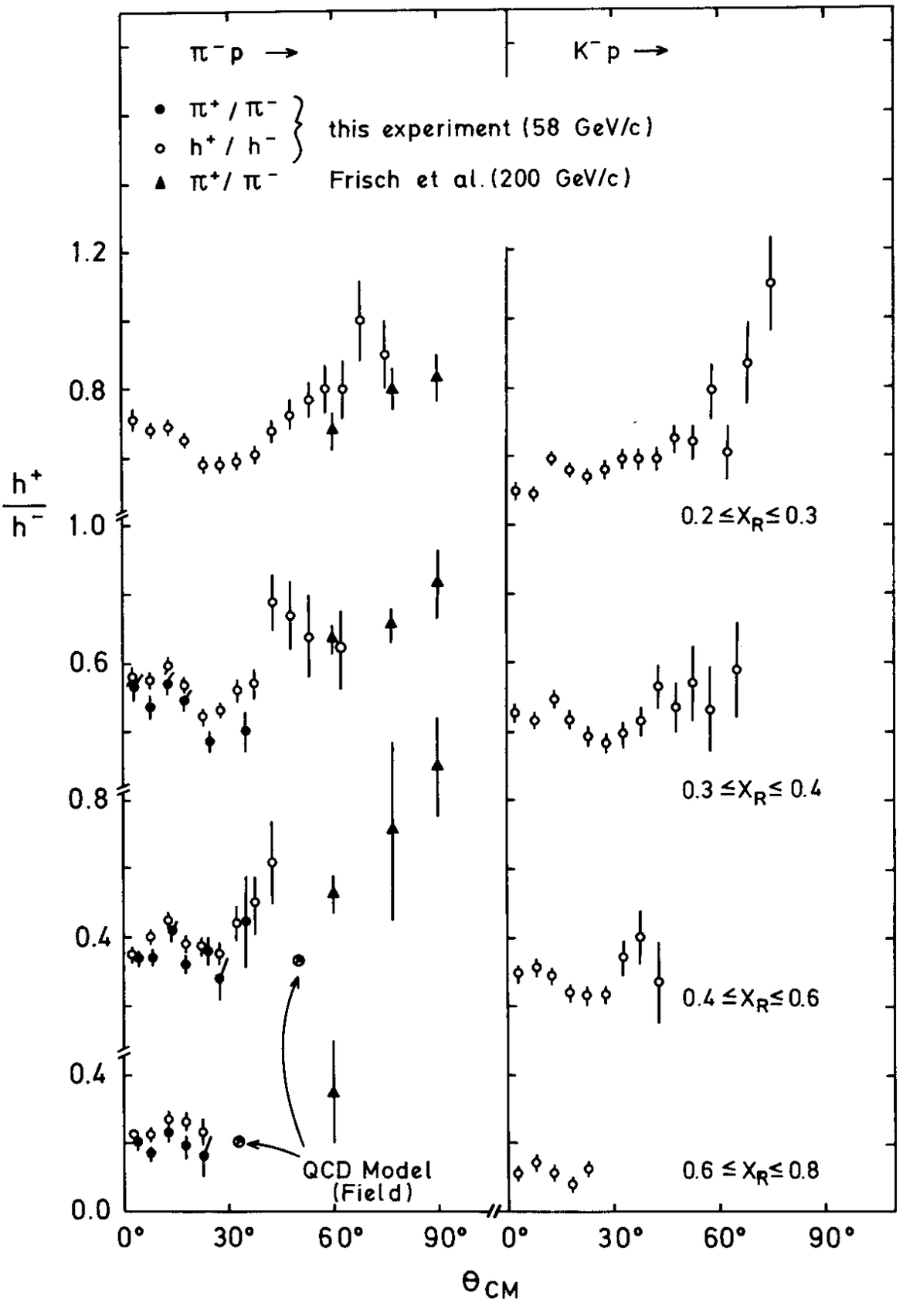
π⁻p →
K⁻p →
π⁺ / π⁻
h⁺ / h⁻
this experiment (58 GeV/c)
π⁺/ π⁻
Frisch et al. (200 GeV/c)
h⁺ / h⁻
1.2
0.8
1.0
0.6
0.8
0.4
0.4
0.0
0.2 ≤ X_R ≤ 0.3
0.3 ≤ X_R ≤ 0.4
0.4 ≤ X_R ≤ 0.6
0.6 ≤ X_R ≤ 0.8
QCD Model
(Field)
0°
30°
60°
90°
0°
30°
60°
90°
Θ_CM

Fig. 21

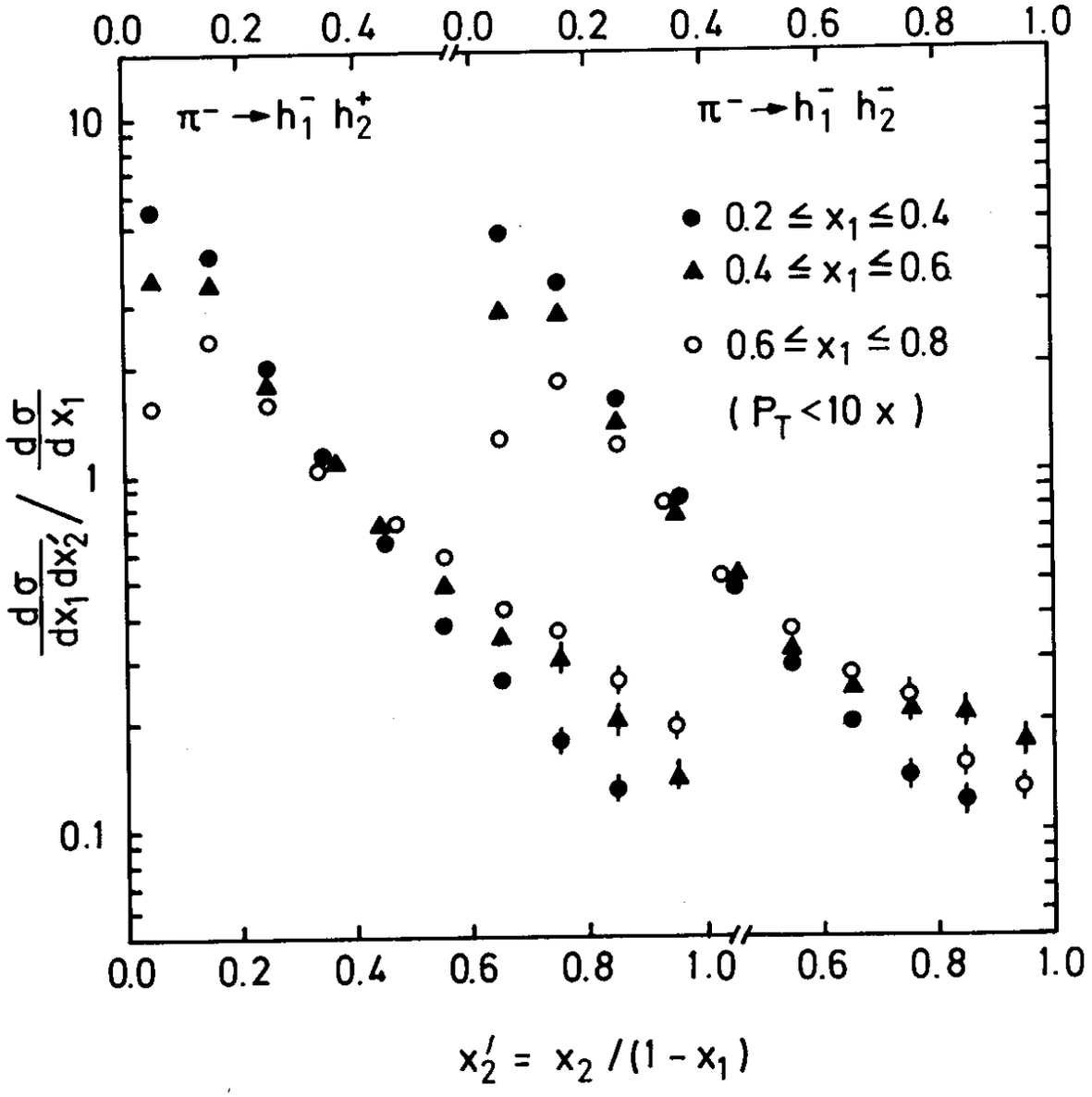
0.0 0.2 0.4 0.0 0.2 0.4 0.6 0.8 1.0
10
1
0.1
$\pi^- \rightarrow h_1^- h_2^+$
$\pi^- \rightarrow h_1^- h_2^-$
$0.2 \leq x_1 \leq 0.4$
$0.4 \leq x_1 \leq 0.6$
$0.6 \leq x_1 \leq 0.8$
$(P_T < 10\ x)$
$\frac{d\sigma}{dx_1 dx_2'} / \frac{d\sigma}{dx_1}$
0.0 0.2 0.4 0.6 0.8 1.0 0.6 0.8 1.0
$x_2' = x_2 / (1 - x_1)$

Fig. 22

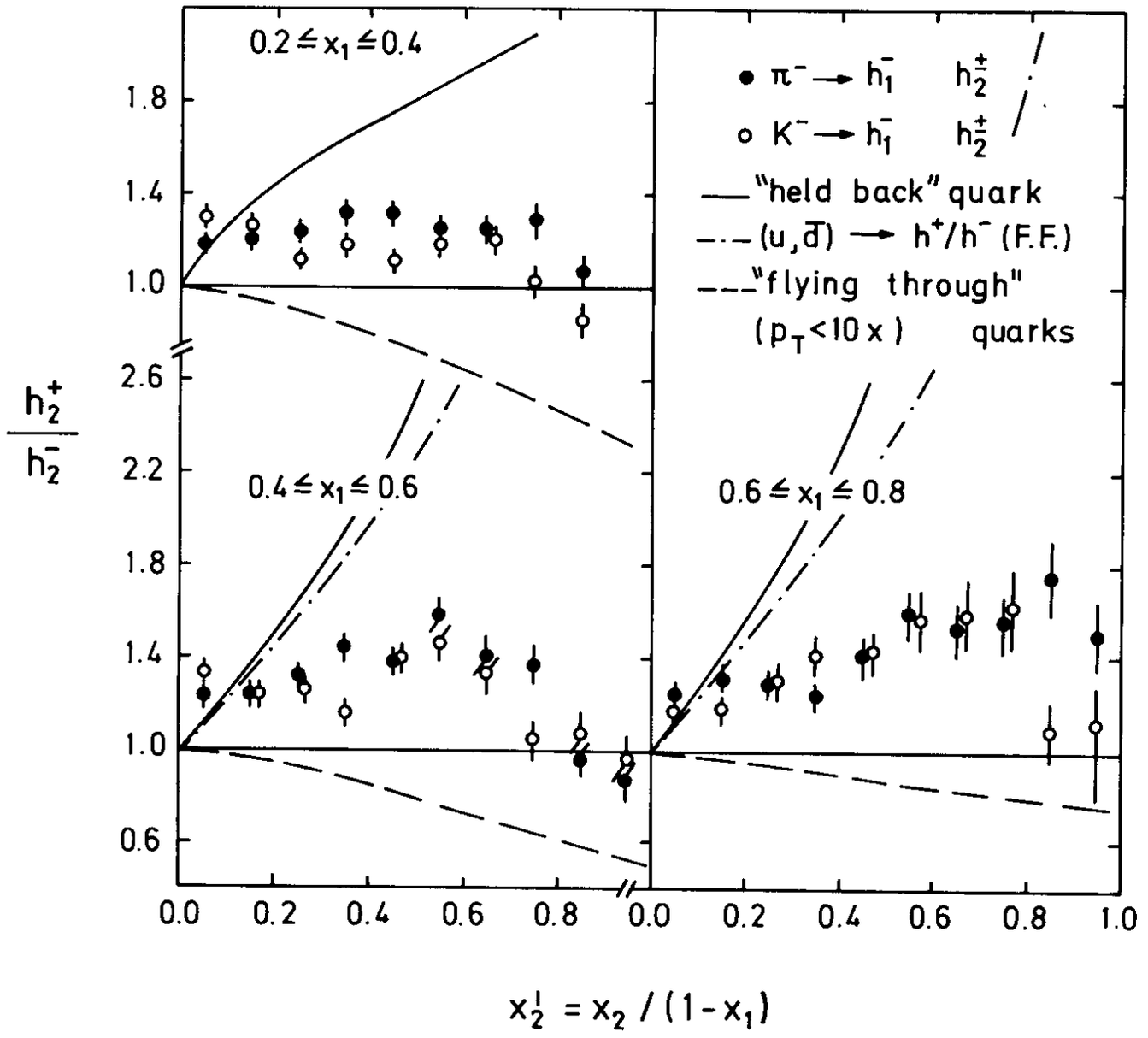
$0.2 \leq x_1 \leq 0.4$
$0.4 \leq x_1 \leq 0.6$
$0.6 \leq x_1 \leq 0.8$
$\pi^- \rightarrow h_1^-$ $h_2^\pm$
$K^- \rightarrow h_1^-$ $h_2^\pm$
"held back" quark
$(u,\bar{d}) \rightarrow h^+/h^-$ (F.F.)
"flying through" ($p_T < 10\,x$) quarks
$\frac{h_2^+}{h_2^-}$
$x_2' = x_2 / (1 - x_1)$

Fig. 23

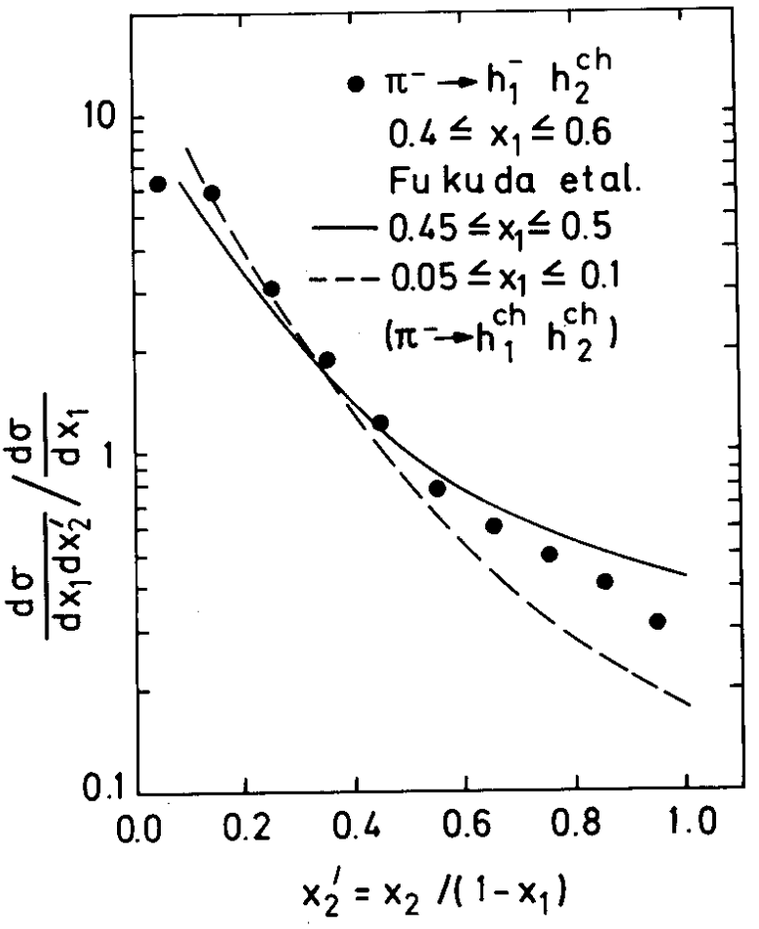
$\pi^- \rightarrow h_1^- \; h_2^{ch}$
$0.4 \leq x_1 \leq 0.6$
Fukuda et al.
$0.45 \leq x_1 \leq 0.5$
$0.05 \leq x_1 \leq 0.1$
$(\pi^- \rightarrow h_1^{ch} \; h_2^{ch})$
$\frac{d\sigma}{dx_1 dx_2'} / \frac{d\sigma}{dx_1}$
10
1
0.1
0.0
0.2
0.4
0.6
0.8
1.0
$x_2' = x_2 / (1 - x_1)$

Fig. 24

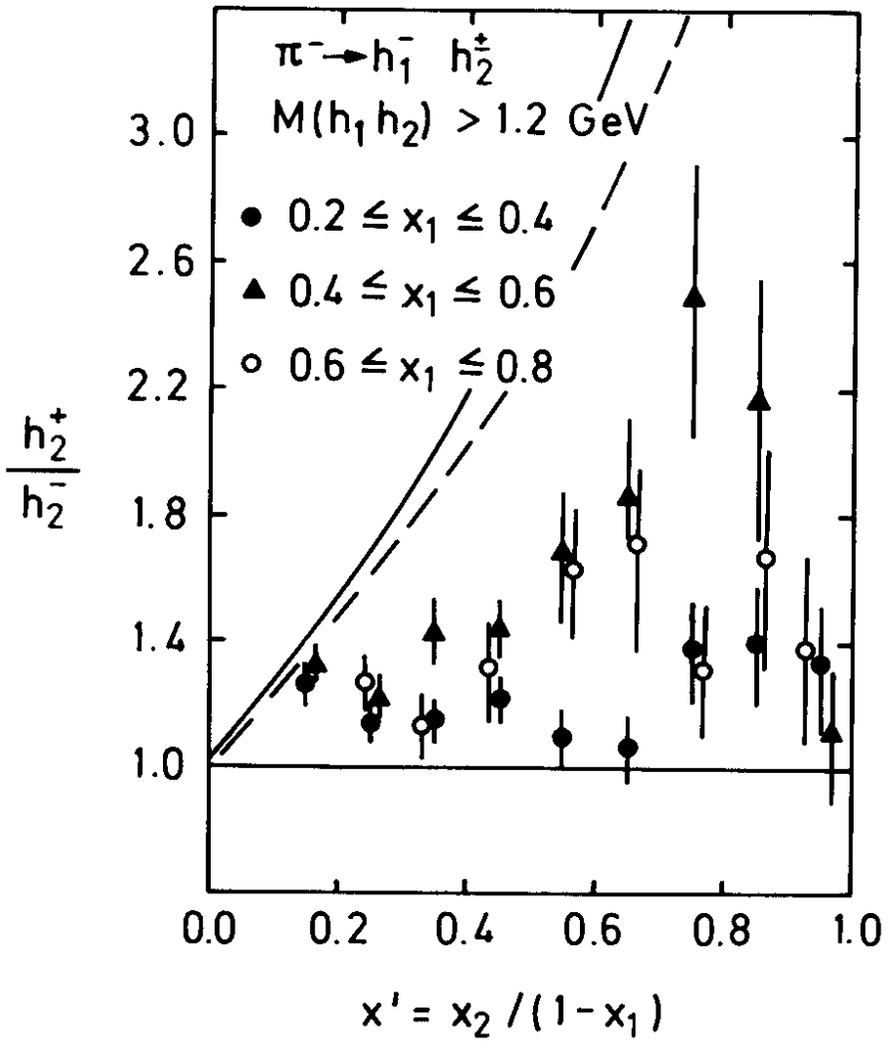
$\pi^- \to h_1^- \; h_2^\pm$
$M(h_1 h_2) > 1.2$ GeV
● $0.2 \leq x_1 \leq 0.4$
▲ $0.4 \leq x_1 \leq 0.6$
○ $0.6 \leq x_1 \leq 0.8$
$\frac{h_2^+}{h_2^-}$
3.0
2.6
2.2
1.8
1.4
1.0
0.0
0.2
0.4
0.6
0.8
1.0
$x' = x_2 / (1 - x_1)$

Fig. 25

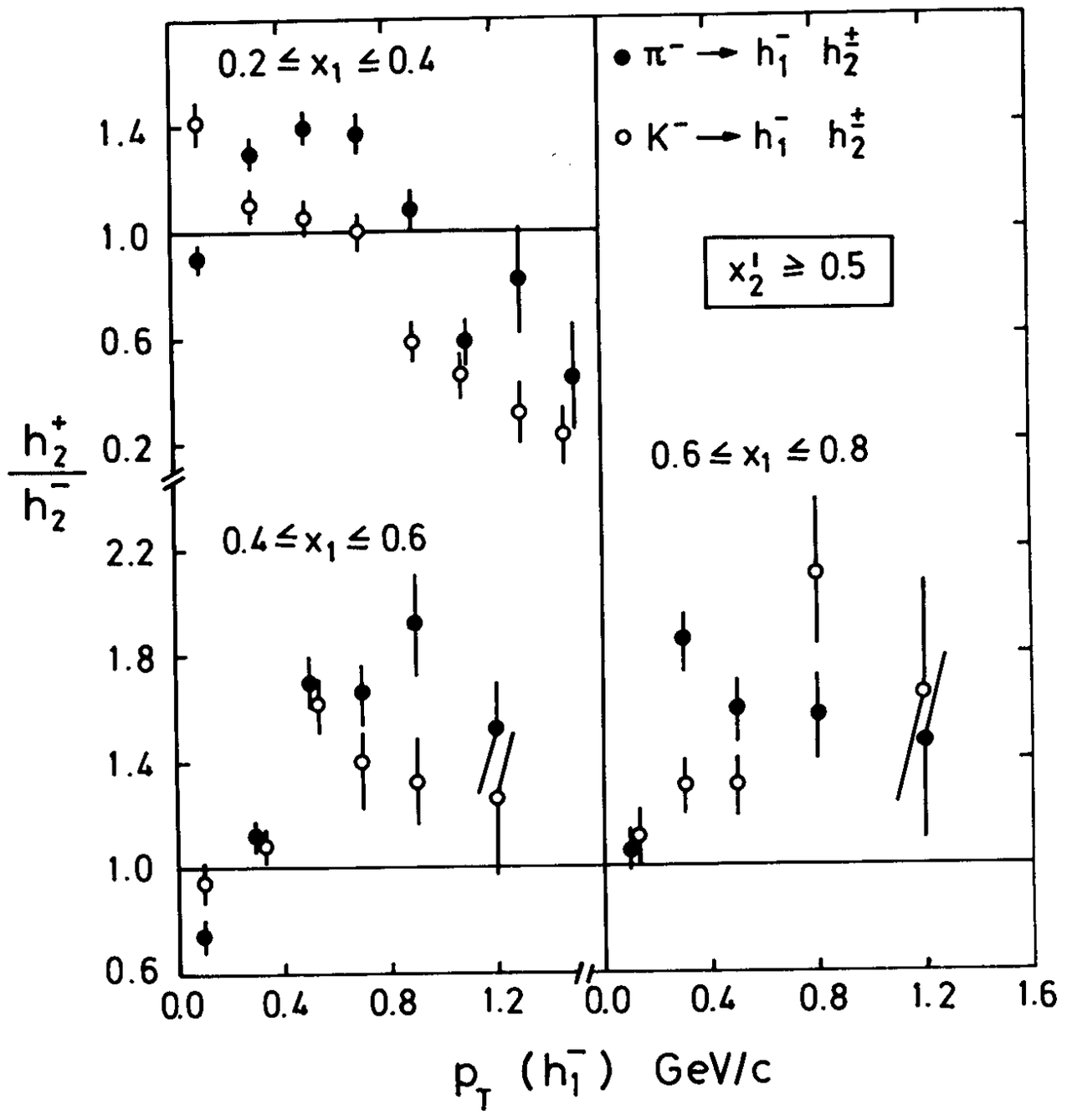
$0.2 \leq x_1 \leq 0.4$
$\bullet\ \pi^- \rightarrow h_1^- \ h_2^\pm$
$\circ\ K^- \rightarrow h_1^- \ h_2^\pm$
$x_2' \geq 0.5$
$0.6 \leq x_1 \leq 0.8$
$0.4 \leq x_1 \leq 0.6$
$\frac{h_2^+}{h_2^-}$
1.4
1.0
0.6
0.2
2.2
1.8
1.4
1.0
0.6
0.0
0.4
0.8
1.2
0.0
0.4
0.8
1.2
1.6
$p_T\ (h_1^-)$ GeV/c

Fig. 26

Druck: Dokumentation Astrophysik Karl-Schwarzschild-Str. 1 · 8046 Garching bei München